UNIVERSITY OF CALIFORNIA
SANTA CRUZ

THE ORIGIN OF THE NET MAGNETIC MOMENT IN $LaCoO_3$

A dissertation submitted in partial satisfaction of the
requirements for the degree of

DOCTOR OF PHILOSOPHY

in

PHYSICS

by

Gregory M. Kaminsky

September 2017

The Dissertation of Gregory M. Kaminsky
is approved:

Professor David P. Belanger, Chair

Professor Frank (Bud) Bridges

Professor David Lederman

Tyrus Miller
Vice Provost and Dean of Graduate Studies

Table of Contents

List of Figures

Abstract

The Origin of the Net Magnetic Moment in $LaCoO_3$

by

Gregory M. Kaminsky

Investigations into the origin of the magnetic moment in $LaCoO_3$ were done. Using mean-field calculations we demonstrate that the presence of just antiferromagnetic interactions is enough to generate a net moment in the system. Metastable states form upon FC. Twinning interfaces in $LaCoO_3$ are examined and their contribution is demonstrated.

Dedication

To my parents, Misha and Ira

Acknowledgments

Prof. David P. Belanger for being a great advisor, patient and knowledgeable. Dr. Alice Durand for answering numerous question that I always had and bearing my various office antics. Brendan Wells for providing help on the Mirabo program. Dr. Feng Ye, Dr. Masaaki Matsuda, Dr. Jun Wang for collecting the neutron diffraction data that started my thesis. Dr. J-Q Yan for growing the LCO samples used in neutron diffraction experiment.

Chapter 1

Introduction

1.0.1 Magnetization

Transition metal oxides with perovskite structures have useful properties such as ferromagnetism, ferroelectricity, giant/colossal magnetoresistance effects (GMR/CMR), and multiferroics (simultaneous ferroelectricity and ferromagnetism), making them good candidates for various devices in electronics and as sensors. One of the more intriguing perovskites, LaCoO3 (LCO), has fascinated researchers for decades. Interactions occurring on similar energy scales, for example, Hunds coupling and crystal field energies, give rise to a variety of competing phases. The magnetic susceptibility of $LaCoO_3$ demonstrates at least two broad transitions near T_1 = 90K and T_2 = 500K. Multiple neutron diffraction studies were done over the years, but no long range magnetic order in $LaCoO_3$ down to 4K [21, 22, 23] has been found. This means that the susceptibility peak at 40K cannot represent the onset of antiferromagnetic (AFM) order from the dominant antiferromagnetic interactions. This susceptibility appears to vary strongly with the strength of magnetic field, the size of $LaCoO_3$ polycrystal/particle (see Fig. 1.1) and doping (substitution Sr in $La_{1x}Sr_xO_3$ in quantities as low as x = 0.002 changes susceptibility drastically especially for T $<$ 37K.[24, 25]

Epitaxial strain and external pressure also have significant effects on magnetization.[26, 16, 27, 28] Nanoparticles of different sizes appear to have different susceptibility as well.[15, 29, 30] Thermal conductivity and electrical resistivity also undergo interest-

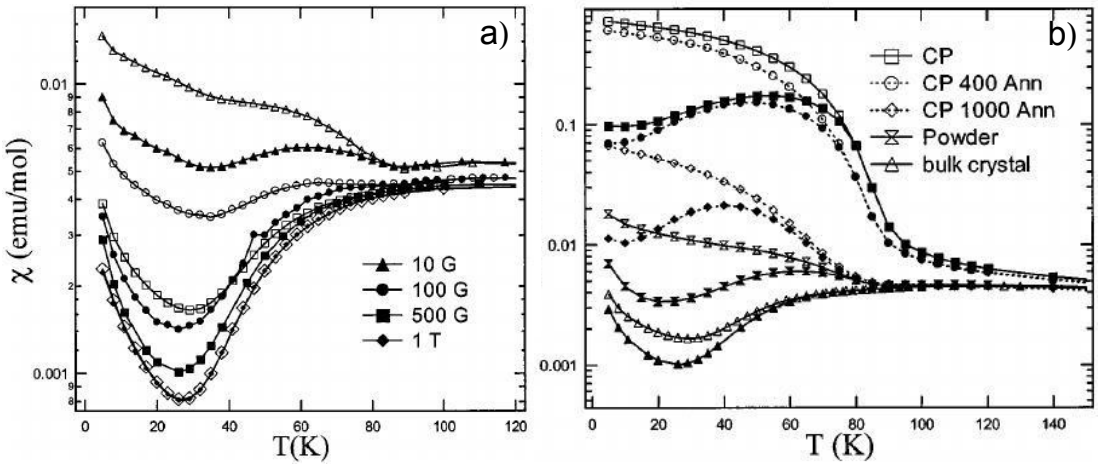

Figure 1.1: a)Magnetic susceptibility vs. temperature of $LaCoO_3$ single polycrystal, ground powder, an unannealed cold pressed (CP) pellet, a CP pellet annealed at 673K and a CP pellet annealed at 1300K, all measured at 500 Oe in ZFC (open) and FC (solid) modes. The number of twins due to strain with the surface might naturally be greater in nanoparticles and unannealed CP pellets, then in the bulk. b) Magnetic susceptibility vs. temperature of $LaCoO_3$ single polycrystal (24mg) in ZFC(solid)and FC(open) modes measured in different fields. Figure taken from Ref. [1]

ing changes in the $10K < T < 300K$ region.[31, 25, 32, 33] Possible sources of magnetic moment are the twinning interfaces that appear in the bulk LCO[34, 5, 35] and possibly in nanoparticles. Putting strain on thin LCO films can create such interfaces near the substrate interface.

1.0.2 Structure

To understand the behaviour of $LaCoO_3$, its structure has to be examined. It is a perovskite material composed of lanthanum, cobalt and oxygen. A perovskite has a general chemical formula ABO_3, where A is a rare-earth or alkali-earth metal (usually with 2+ or 3+ valence) and B is a transition metal (usually 3+ or 4+ valence). Oxygen ions form an octahedron around each B atom, with 8 corner sharing octahedral around each A rare-earth. The ideal perovskite structure is cubic, as seen in the Fig. 1.2. In such a construction, the Co-O-Co angle is 180° and the bond length Co-O is the same for all six bonds on the cobalt octahedra.

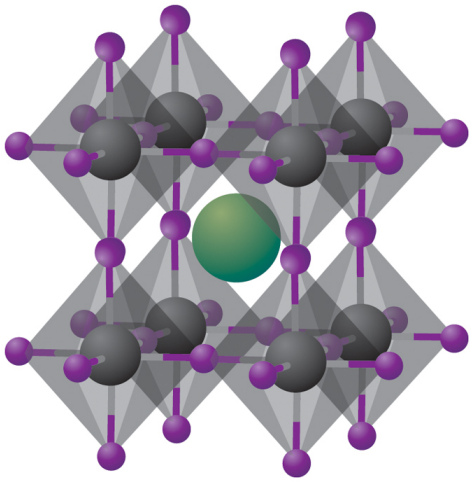

Figure 1.2: Image of the Ideal Cubic perovskite structure. Green is A the rare-earth, Grey is B the transition metal and Purple is the oxygen atom. In this image the B-O-B angle is 180°. Figure was taken from Ref. [2]

In the case of lanthanum cobalt oxide, the rare-earth is La and transition metal is Co. LCO is rhombohedrally distorted especially at low temperature. The cobalt octahedra are twisted with respect to each other, with the Co-O-Co angle being approximately 163° (instead of 180° in an ideal cubic lattice, see Fig. 1.3). The oxygen atoms are displaced toward lanthanum. This action reduces the total volume of the unit cell without changing the Co-O bond length. The twist can be changed upon doping, substituting strontium (Sr) or calcium (Ca) for La. This changes Co-O-Co angle to be closer to the ideal cubic structure[36] (due to the larger size of Sr vs. La for example).

Doping by an element with a smaller ionic radius than La, such as gold (Eu), creates an opposite effect, reducing the Co-O-Co angle,[37] as does increasing the external pressure. Unlike the Co-O-Co angle, the cobalt octahedra appears to be very stable, with the Co-O bond length remaining the nearly same with temperature or doping.[38, 39, 40]

As it cools the LCO lattice undergoes transition from cubic to rhombohedal phase. The stress that accompanies this transition is relieved by deformation twinning. The most common twinning interfaces are (1 0 0) and (1 1 0) in pseudocubic coordinates

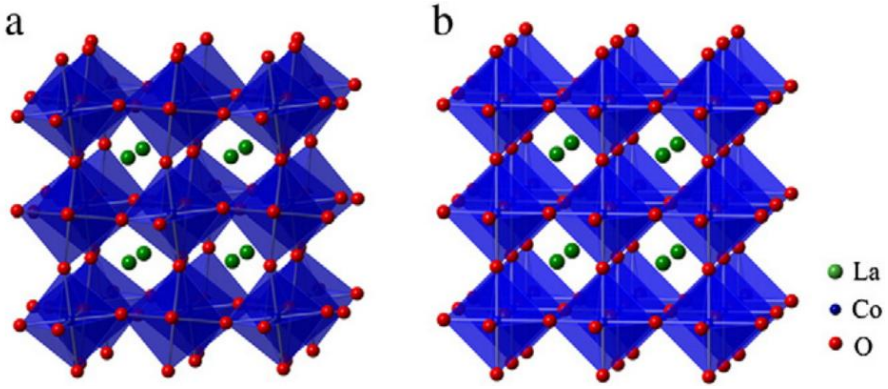

Figure 1.3: Lanthanum Cobalt Oxide. On the right is the ideal cubic and on the left is the rhombohedral distortion. Figure was taken from Ref. [3]

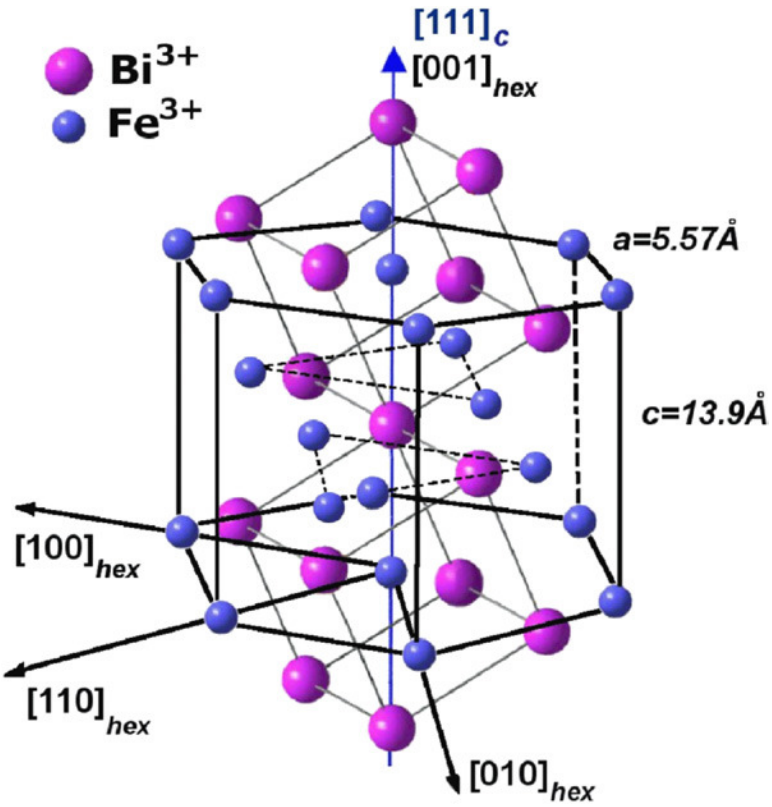

Figure 1.4: Hexagonal and pseudocubic coordinates displayed on an image of BiFe. LCO has similar structure as BiFe. Pseudocubic coordinates can be seen by looking at the cube of Bi^{+3}[4]

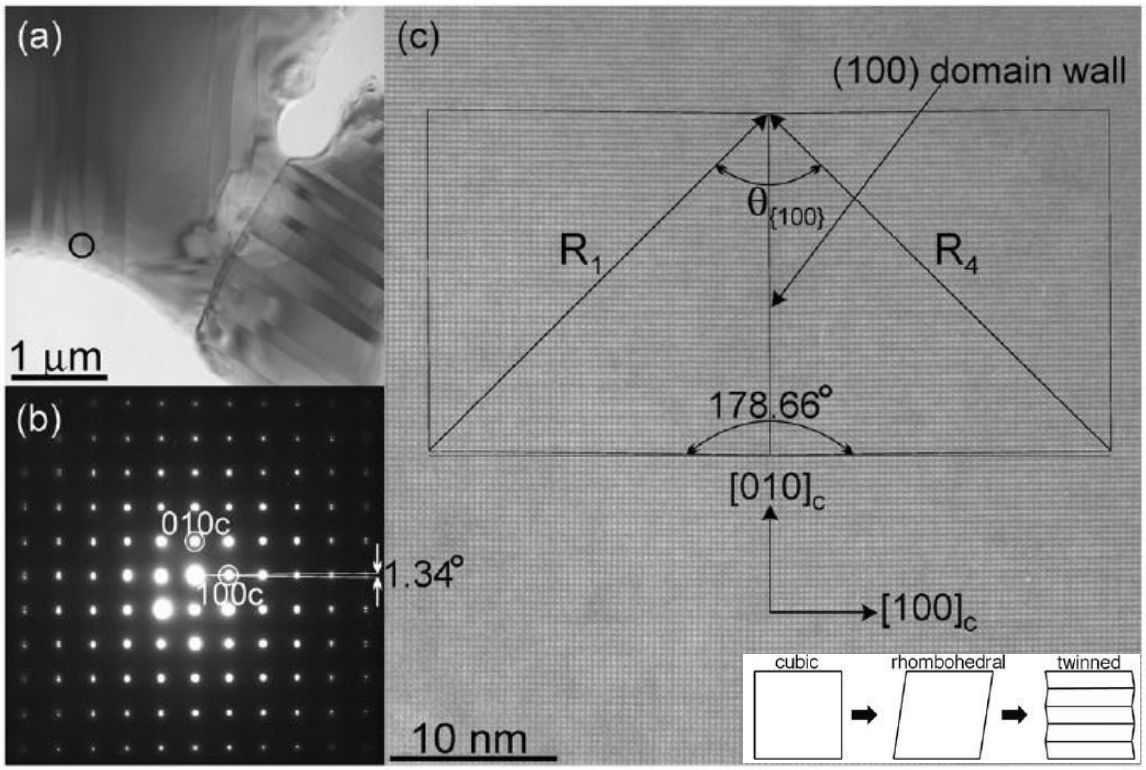

Figure 1.5: a) (1 0 0) twins with a common grain boundary. b) Diffraction pattern recorded with a small area diffraction aperture centred on a (1 0 0) domain wall. c) Rombohedral distortion due to a break from cubic symmetry. In pseudocubic coordinates $R_1 = [111]$ and $R_4 = [\bar{1}11]$ with a 'c' subscript on the image indicating pseudocubic (hexagonal and pseudocubic coordinates displayed in Fig. 1.4). Figure taken from Ref.[5].

(see Fig. 1.4).[34, 5, 35] Twinning interfaces (1 0 0) are more common. In a similar rhombohedrally distorted perovskite LaAlO3 (LAO), it was shown by Kim et al.[41] that (1 0 0) twinning creates smaller strain than (1 1 0) twinning and, thus, is energetically more favorable. The twins are stable at room temperature.[34] We used a crystallographic imaging program called Mirabo to examine twinning at a (1 0 0) interface and the unusual pattern of Co-O-Co angles that occurs at this interface (see Fig. 3.1, Fig. 3.2, Fig. 3.3, Fig. 3.4).

1.0.3 HS vs. IS vs. LS

Focusing on the cobalt octahedra, we now discuss what is happening on the cobalt ion. Co is a 3d transition metal with electron configuration $[Ar]3d^74s^2$. Possible valence states are 5d electrons (4+), 6d electrons (3+) or 7d electrons (2+). In $LaCoO_3$, the valence is [3+],[42] which means that six electrons are distributed among 5 orbitals, two on-axis orbitals (e_g) and three-off axis orbitals (t_{2g}). For the cobalt inside the octahedra, on-axis orbitals will be higher in energy due to repulsion of the 2p electrons from the oxygen. The ligand splitting, $10D_q$ (crystal field splitting), is 0.9 ± 0.3 eV.[43] The difference between crystal-field splitting and the Hund's exchange energy is estimated to be $E \approx 50$meV.[7]

The lowest energy configuration is the low spin (LS) state, where all six electrons occupy t_{2g} orbitals with two electrons per orbital leaving no unpaired electrons; this state is diamagnetic. The high spin state (HS) is another possibility with two electrons occupying two e_g orbitals. In accordance with Hund's rule, those two electrons would occupy two different orbitals (both on axis orbitals are occupied now), with the spins aligned. A third possibility, suggested by LDA + U calculations by Korotin et al.,[44] is an intermediate spin state (IS), with only one electron in the e_g orbital. See Fig. 1.7, or Fig. 1.8. Because the LS state is diamagnetic, according to single ion picture, any source of magnetic moment must be either from IS or HS states (or a combination of both).

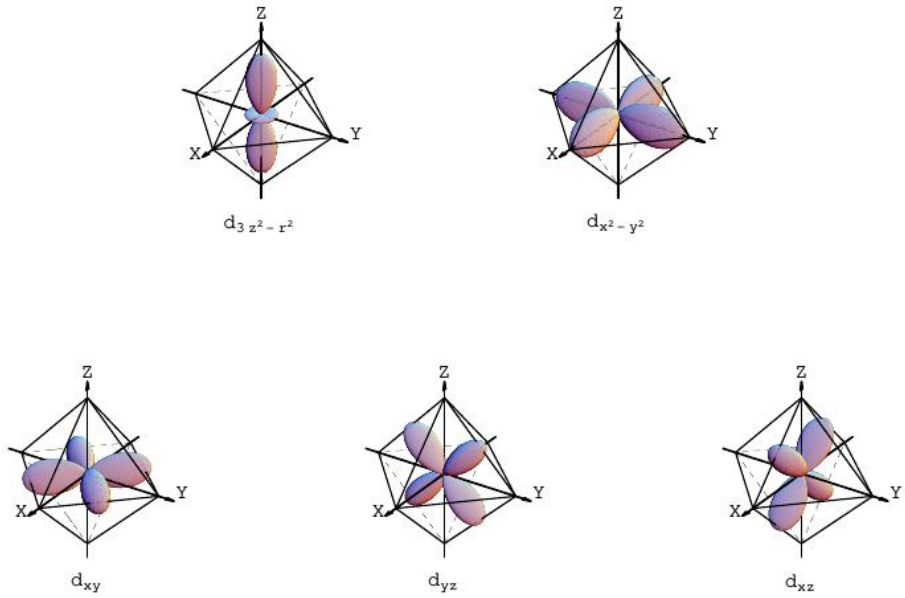

Figure 1.6: Bottom - t_{2g}, top - e_g orbitals. Since e_g orbitals point in the direction of oxygen p orbitals, they are higher in energy.

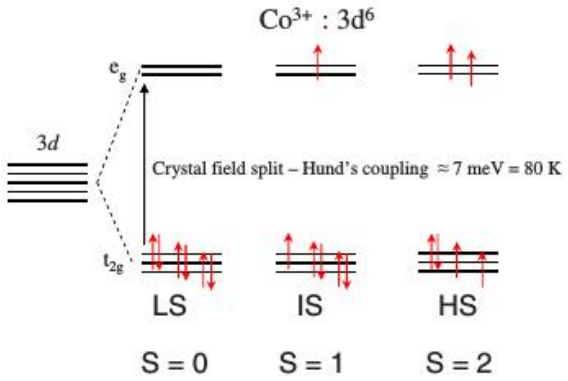

Figure 1.7: LS, IS, HS states.[6] The difference between Δ_{CF} and J_{EX} is not 7meV as displayed in this image, but $\Delta_{CF} - J_{EX} \approx 50$meV.[7] Figure was taken from Ref. [6]

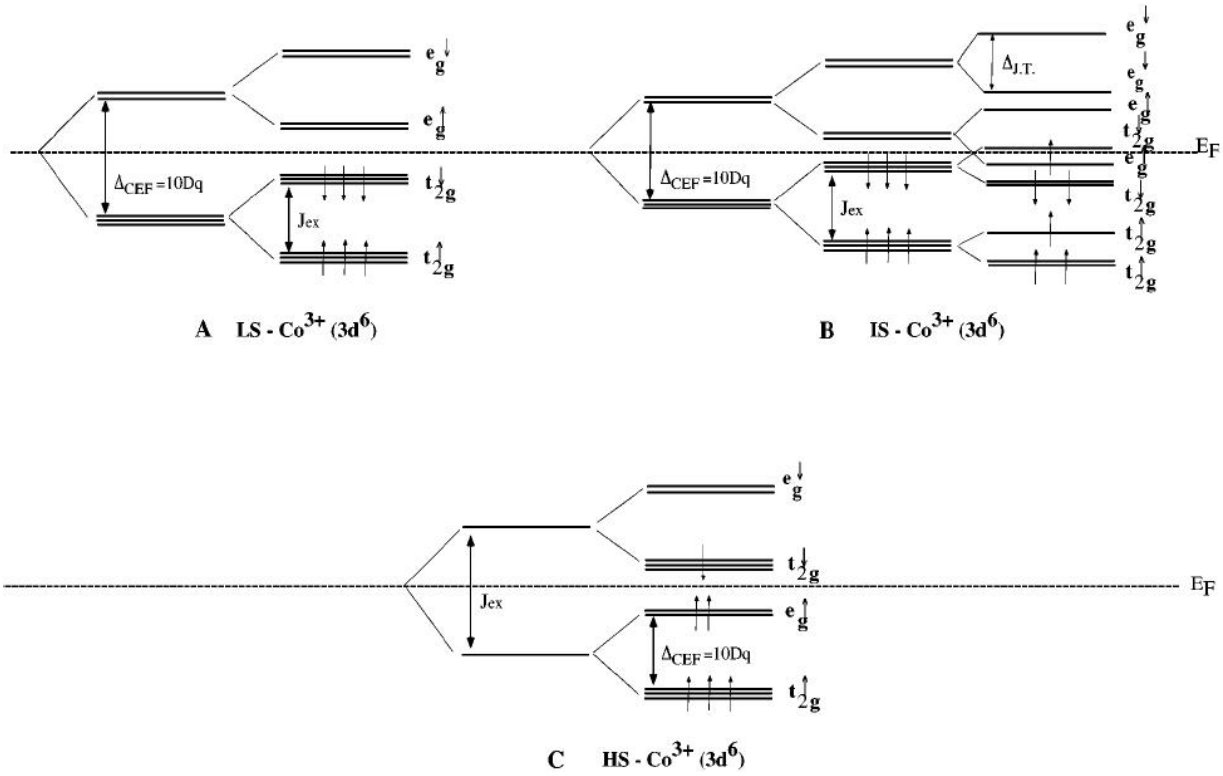

Figure 1.8: Diagram of LS, IS, HS spin states. The orbitals e_g are higher in energy the t_{2g} orbitals due to repulsion from oxygen p-orbitals. For HS state, the energy of e_g orbitals is lowered by Hund's exchange coupling. For IS state the energy of one of the e_g orbitals is lowered by JT-like distortion. Figure taken from Toulemonde et al.[8]

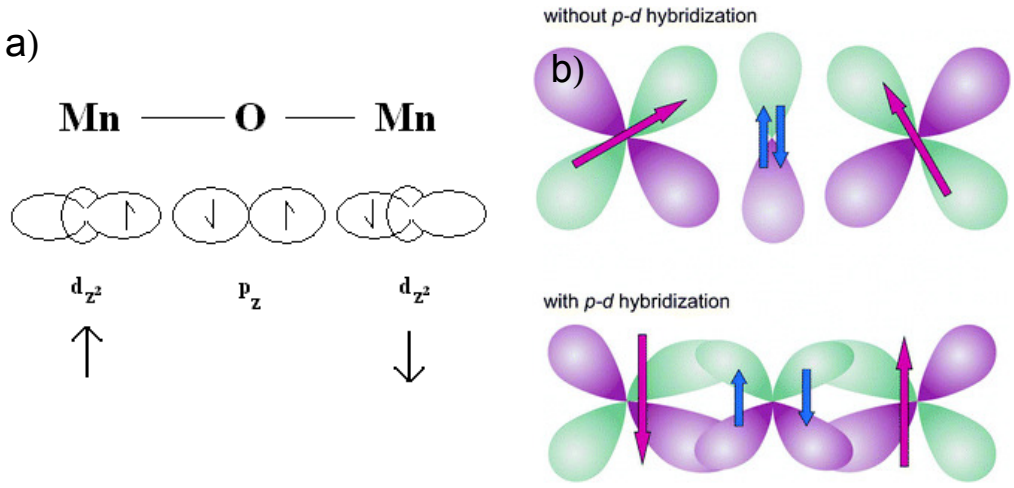

Figure 1.9: a)The superexchange interaction for two manganese ions mediated by oxygen.[9] The d orbitals of the manganese are hybridized from d to p type orbitals. Mn-O-Mn angle is 180°. Figure was taken from Ref. [9] b)Another view of the superexchange interactions. Tilting the transition ions away from 180° must reduce the symmetry, hence weakening the interaction. Figure taken from Ref. [10].

1.0.4 Double exchange, Superexchange

Superexchange is an antiferromagnetic interaction between two magnetic cations separated by a non-magnetic anion. Electrons on the cation atom d-orbitals couple with electrons on the anion p orbital. The cation-anion-cation angle in a superexchange interaction is usually 180°, as depicted in Fig. 1.9. Here, the p orbitals from the oxygen and d orbitals from the donor atom form a direct exchange, lowering kinetic energy of the system by de-localizing electrons in the p and d orbitals. In the strong interaction approximation, the Hubbard Hamiltonian for the system is

$$H_{1,2} = \frac{2t}{U}\overrightarrow{S_1} \cdot \overrightarrow{S_2}, \tag{1.1}$$

with t being the hopping energy between d and p orbitals and U being the Hubbard energy for the donor atom. As a singlet state is energetically favoured, such an interaction is antiferromagnetic. According to the Goodenough-Kanamori rules, antiferromagnetic interactions work best with both cobalt ions in HS state, where 2 electrons in the e_g orbital couple with electrons in the p orbitals of the oxygen with

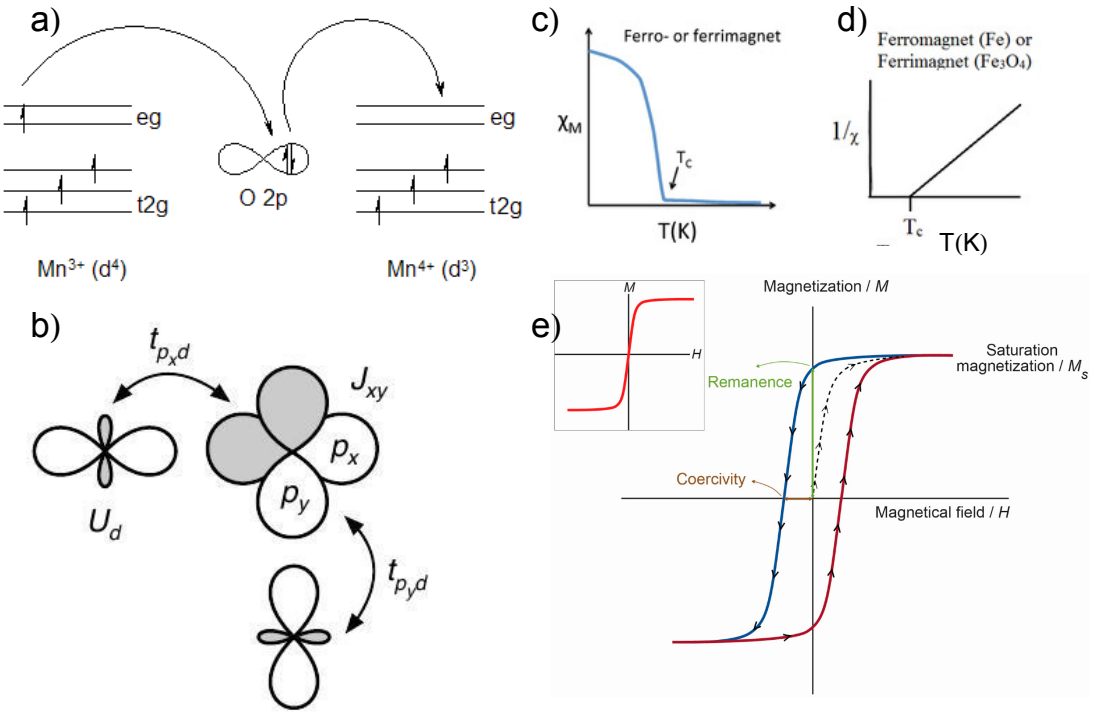

Figure 1.10: a)Double exchange interaction. Such interaction can only occur if unequal number of electrons exist on the two transition ions. Figure taken from Ref.[11] b)P-d orbital interaction diagram. The p are the orbitals on the oxygen ion interacting with the d orbitals on the transition ion (TI). The TI-O-TI angle is 90° in this image. Figure was taken from Ref. [12] c)Susceptibility diagram for a ferromagnetic, T_c is the ferromagnetic transition temperature. d)Inverse susceptibility for a ferromagnet. Note, the intersection with x-axis occurs for positive T. d)Hysteresis, can only exist with ferromagnetic interactions.

the e_g undergoing d-p hybridization. (See Fig. 1.9).

Double exchange is a ferromagnetic interaction between cations that are in different oxidation states. Electron hopping from one donor atom to another (mediated through the p_σ orbital of the oxygen) lowers the kinetic energy of the system, akin to superexchange. According to Hunds rules, the largest value of spin angular momentum has the lowest energy, thus aligning the spins on each ion. Such an interaction requires unequal number of electrons to exist on the e_g orbitals of the transition ions (see Fig. 1.10).

1.0.5 Why the IS state?

Two cobalts in in different oxidation states mediated by oxygen can enable ferromagnetic interactions. Goodenough[42] discusses the effects different valences and spin states would have on magnetic interactions.

The possible states are

1. Co_{3+}^{LS} $(t_{2g}^6 e_g^0)$
2. Co_{3+}^{HS} $(t_{2g}^4 e_g^2)$
3. Co_{4+}^{LS} $(t_{2g}^5 e_g^0)$
4. Co_{4+}^{HS} $(t_{2g}^5 e_g^0)$

and the possible interactions are

- Co_{3+}^{LS} - O - Co_{3+}^{LS} non-magnetic, all paired electrons
- Co_{3+}^{LS} - O - Co_{3+}^{HS} non-magnetic, as Co_{3+}^{LS} is diamagnetic and doesn't interact
- Co_{3+}^{LS} - O - Co_{4+}^{LS} non-magnetic
- Co_{4+}^{LS} - O - Co_{4+}^{LS} antiferromagnetic
- Co_{4+}^{LS} - O - Co_{3+}^{HS} ferromagnetic
- Co_{3+}^{HS} - O - Co_{3+}^{HS} antiferromagnetic

At first glance, ferromagnetic states appear to be possible, but they require 4+ valence on the Co. According to X-ray absorption spectra (XAS) study[43, 39] the valence is found to be 3+ below room temperature (this does not preclude a very small amount of Co with 4+ valence). A different model to obtain ferromagnetism was devised by Korotin et al.[44], invoking an intermediate state (IS). In such a scenario Co^{HS} - O - Co^{IS}, Co^{IS} - O - Co^{IS}, Co^{LS} - O - Co^{IS} all can work. Low temperatures, at $T < 50K$, correspond to LS occupied state. A gradual transition to IS and later possibly HS states would take place at higher temperatures. This model

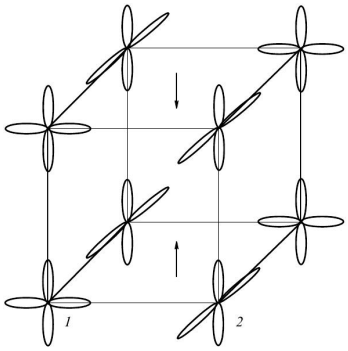

Figure 1.11: Diagram of intermediate spin state in LCO. One e_g orbital contains one spin only. Missing on this image are the atoms of oxygen, whose p orbitals are suppose to mediate the interaction. Important to note - the angle between the cobalt and oxygen here is 180° and not 90° as in fig. 1.10. Figure was taken from Ref. [13]

also explains the metallic-like behaviour of $LaCoO_3$ for the temperature regime 90K $<$ T $<$ 500K.[44]

Since only one of the e_g orbital is occupied in the IS state (see Fig. 1.11), there must be a Jahn-Teller-like distortion in the octahedra. Elongating the Co-O bond increases the distance between cobalt $d3z^2$ - r^2 and oxygen p orbitals, lowering the repulsion energy.

This model appears to be logical and consistent, but experimental evidence does not support it. According to pair-distribution function (PDF) studies done via neutron scattering and extended X-ray absorption fine structure (EXAFS), which examined the range of bond lengths in $LaCoO_3$,[26, 39, 45] no significant Jahn-Teller distortion was found. While a paper by Maris et al.[46] claimed to find evidence for I2/a space group using X-ray diffraction data, allowing for a cooperative JT distortion, those finding are contradicted by other Rietveld refinement measurements which better support the $R\bar{3}c$ group,[45] indicating no significant JT exists.

NMR ^{59}Co and ^{159}La Knight shift measurements are temperature independent below 30K,[47] demonstrating a lack of any magnetic interaction below 30K. A single ^{159}La spin-echo signal was observed for 4.2K $<$ T $<$ 300K, and the authors interpret this to mean that only a single magnetic state exists at any one time below 300K, because both the HS and IS states are magnetic, a mixture of them is ruled out

(assuming an IS state even exists).

Soft X-ray absorption and magnetic circular dichroism (MCD) of the Co-$L_{2,3}$ edge revealed that the spin state transition at T $\approx$ 50K is well described by an LS ground state and triply degenerate HS excited state.[7] A mixture of IS-HS is still possible, but only at very low levels. The g-factor was measured to be g = 3.2.[7] Inelastic neutron scattering results[24] determined that the g-factor g $\approx$ 3 and an electric spin resonance study[25, 48] supports a g-factor of 3.35-3.55. This is in agreement with the predictions for HS spin state.[49]. Since there is only one electron in the e_g orbital, the predicted g $\approx$ 2.0 for the IS state is in disagreement with the data. Hartree-Fock calculations demonstrate that the HS state or the HS-LS ordered state is more stable than the IS state.[50] XAS Intensity changes in pre-edge region are consistent with a transition from a lower to a higher spin state.[51] We can assume with reasonable certainty that the 50K anomaly is the activation of the transition from LS to HS state, in the single ion picture that is, but there are indications that this picture is not entirely valid for $LaCoO_3$. Medling et al.[52] argue that the broad range of e_g density of states as seen in LDA calculations means that it is better to view LCO in terms of bonding-antibonding states, instead of t_{2g} and e_g states. Then, the magnetic moment is controlled by the Co-O-Co bond angle;

LDA and GGA calculations confirm that magnetic state becomes the lowest energy state with an increase in Co-O-Co angle α.[14] In their paper $\delta x = r \sin \alpha/2$, with r being the bond length Co-O. They demonstrate that smaller δx the energy of the magnetic state goes below the non-magnetic state. The insulating tendency becomes stronger with increasing δx, the rhombohedral distortion.[14] A conclusion supported by resistivity measurements is that a steep rise at T > 200 is connected with increasing δx.[53] Doping with very small amounts (x = 0.002) of Sr (or Ca) changes the resistivity, introducing a large plateau between 200K-400K.[33, 25] It is suggested that, around individual Sr/Ca sites, change in δx creates 12 magnetic bonds nested in non-magnetic material(HS in the single ion picture). The enhanced conductivity might explain the plateau.

A significant hybridization, Co(4p) - O(2p) - Co(3d), is detected in RXES and EXAFS measurements.[54, 55] A greater hybridization of the cobalt 3d into a 4p-type

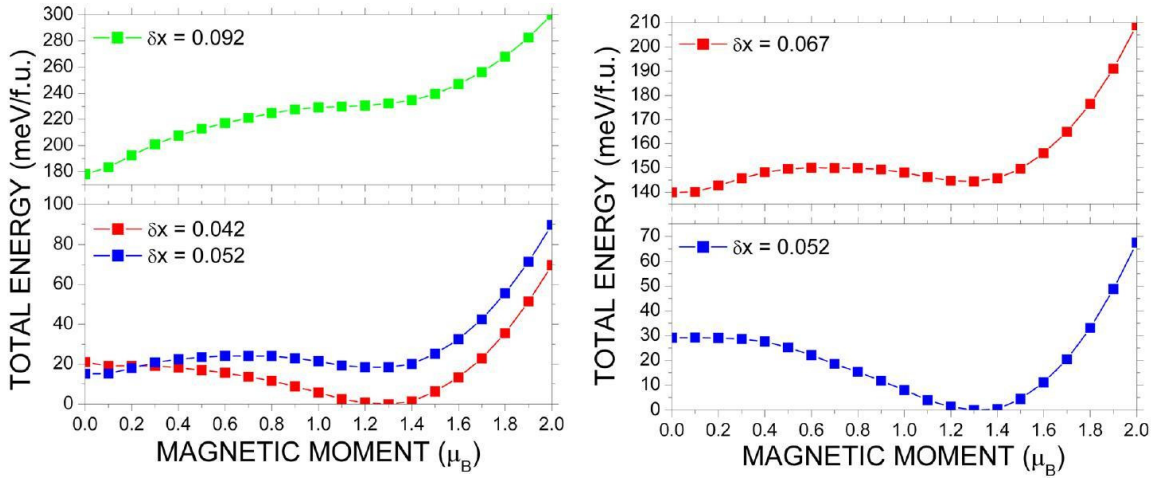

Figure 1.12: a)GGA calculations. Decreasing distortion δx lowers the energy of the magnetic state. b)LDA calculations, the same result as GGA.[14] Although Lee et al.[14] do not say whether the magnetic interactions are of the superexchange type, it is difficult to see how any other interaction can occur. Figure was taken from Ref. [14]

orbital would make sense if the interactions are of the superexchange type. As mentioned previously, the cobalt octahedron itself is very stable and Co-O length stays relatively constant across a wide range of temperatures. It is the Co-O-Co angle between neighbouring octahedra that undergoes a significant change with temperature, pressure, doping or strain. Larger angles correspond to greater 3d-4p hybridization consistent with measure.[51, 54, 55]

There is competition between crystal field splitting Δ_{CF} of the Co(3d) e_g and t_{2g}, states that favors the LS configuration, and the Hund exchange that favors HS configuration. Following Sterbinsky et al.,[55] the energy difference between the two configurations, $e_g - t_{2g} = \Delta$, is created by the competing interactions of crystal field splitting Δ_{CF} and Hund's exchange coupling, with $\Delta = \Delta_{CF} - W/2$, where W is the energy related to the overlap between Co(3d) derived e_g and O(2p) orbitals. The overlap W and crystal field splitting Δ_{CF} are dependent upon Co-O-Co angle α and Co-O distance r_{Co-O}, with

$$W \propto r^{-3.5}\sin(\alpha/2) \tag{1.2}$$

$$\Delta_{CF} \propto r^{-5}. \tag{1.3}$$

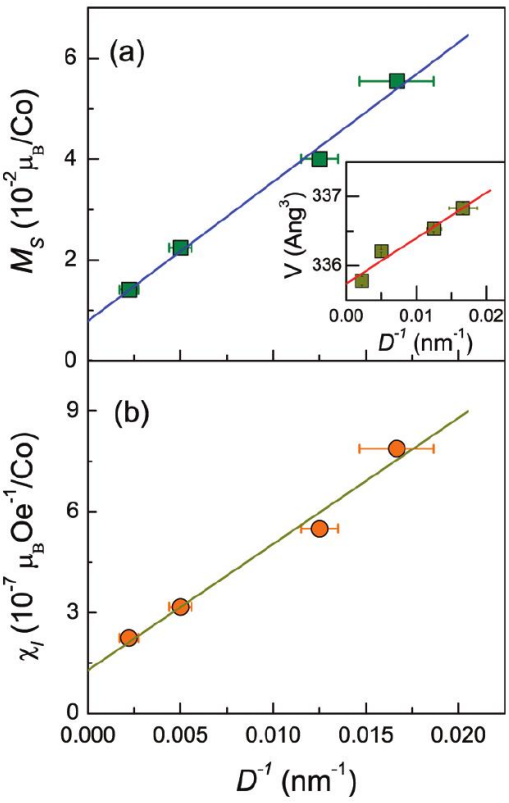

Figure 1.13: Susceptibility vs. diameter relationship.[15] Extrapolation of a saturated M_S is found that is close to that of the bulk $LaCoO_3$. Figure was taken from Ref. [15]

The r_{Co-O} distance remains approximately constant in LCO; the other parameters though change. Unbending of Co-O-Co angle reduces the energy gap between between e_g and t_{2g} levels, increasing hybridization between Co(3d) and O (2p) states, favoring the HS state.[55, 56]

1.0.6 Nanoparticles

There have been several investigations of magnetism in $LaCoO_3$ nanoparticles. As with the bulk, no significant JT is detected in nanoparticles. Smaller size often appears to correspond with increasing magnetic moments.[15, 29]

At the same time, the average volume of the unit cell increases with a decrease in particle size.[57, 15, 58] There appears to be a relation between magnetic moment and diameter M $\propto$ 1/D.[30, 15] Impurity contributions from Co_3O_4 also appear to

enhance the net moment[59]. The mechanism might be an increased strain on the Co_3O_4 and LCO interface. According to Harada et al.[58] there is a strong surface component to the moment, possibly enhanced by hole doping on the surface,[58, 1] but the surface component cannot be the main contributor to the moment in the nanoparticles. For a constant volume sample, a pure surface contribution will lead to a moment vs. diameter relation $M \propto 1/D^2$, not what was found. Investigations by Durand et al.[29] showed a drastic difference that the presence of Co_4O_3 impurity has on the magnetic moment. A significantly larger moment was discovered with an increase in Co_4O_3 impurity concentration. It is possible that magnetic moment is affected neither by the size of the nanoparticle, nor by the surface area, but by the amount of strain and faults that LCO has. Extremely small particles of Co_4O_3 must contribute to the strain. Decreasing the size of nanoparticles creates greater strain and could increase the number of twinning interfaces. This might be the reason for increased magnetic moment connected with decreasing size.

LCO has also been grown in the form of nanowires.[60] In such a state, unit cell volume and Co-O-Co angle increase with decreasing diameter of the wires. A clear enhancement of magnetic moment with decreasing diameter exists. The Curie temperature though, remains constant.[60]

1.0.7 Strain

Numerous experiments indicate that putting a strain on LCO films significantly increases the magnetic moment. LCO films were grown on different lattice substrates. The pseudocubic lattice parameter of LCO is $a_b = 3.801\mathring{A}$ (see Fig. 1.4). Growing thin films of LCO on substrates with positive lattice mismatches increases the magnetic moment. Fuchs et al.[35] grew LCO on films on substrates with mismatches of 1.31% for $SrLaAlO_4$, 0.52% for $LaAlO_3$, +1.05% for $SrLaGaO_4$, +1.84% for $(LaAlO_3)_{0.3}$ $(Sr_2AlTaO_6)_{0.7}$ and +2.63% for $SrTiO_3$; the size of the magnetic moment correlates well with the size of the mismatch. It is important note that while the unit cell expanded, the Co-O length remained approximately constant.[56] It is the Co-O-Co angle that is changing (same as in nanowires), as the cobalt octahedra rotate closer to

180° with increasing strain (movement of the octahedra toward a more cubic formation is another way to visualize it).[61]

X-ray absorption spectroscopy (NEXAFS) spectra for polycrystalline LCO (p-LCO) were compared to spectra for LCO grown on $(LaAlO_3)_{0.3}$ $(Sr_2AlTaO_6)_{0.7}$ (LSAT) substrate - epitaxially strained LCO (e-LCO). NEXAFS spectra at the Co $L_{2,3}$ edge for p-LCO appear to change with temperature; 50K, 300K, 450K all differ, possibly indicating a spin transition from LS-HS spin states or increase in the number of d-p hybridization bonding states.[52] In contrast, spectra for e-LCO appear to be stable with temperature as indicated by data at 30K, 300K and 450K.[26] Epitaxial strain appears to stabilize states that correspond to magnetic moment.

An interesting experiment by Choi et al. consisted of a triple layer deposition. Three layers were: $SrTiO_3$ (STO) with a pseudocubic lattice constant $a = 3.905\mathring{A}$ (see Fig. 1.4), LaCoO3 (LCO) lattice constant $a = 3.801\mathring{A}$ and a $SrCoO_2$ (SCO) with a pseudo-tetragonal lattice constant $a_t = 3.905\mathring{A}$. Any LCO grown on either SCO or STO would experience positive strain. The deposition was done with LCO/SCO/STO and SCO/LCO/STO. The sandwiched LCO layer, strained on both sides (SCO/LCO/STO) had a larger magnetic moment.

It is also possible to control the moment dynamically. LCO thin film has been grown with a piezoelectrically stimulated $SrTiO_3$ film. LCO and $SrTiO_3$ films are sandwiched by a thin layer of insulating SiO_2. It also puts additional strain on LCO film. Silicon was the substrate for the films. Metal Ti/Au contacts were deposited on SiO_2. Changing the voltage on the contacts stimulates $SrTiO_3$ film and changes the strain on LCO film, switching the moment on and off.[62]

If expansion of LCO unit cell increases the magnetic moment, what if the unit cell were to shrink? Application of hydrostatic pressure has been shown to significantly reduce magnetic moment in LCO nanoparticles.[57] Doping with gold atoms or substituting Eu for La, shrinks the unit cell and decreases Co-O-Co angle. This reduces the magnetic moment measured.[37] The opposite effect can be achieved by doping with Sr; it has a bigger ionic radius than La. Doping with Sr causes cobalt octahedra to rotate toward a more cubic formation in the bulk material, increasing the average angle[63] and the moment.

According to measurements in LaCoO3 nanoparticles, the average Co-O-Co angle remains constant with increasing temperature, until about 37.5K. Then, there is a power-law type transition[59] and the measured volume of the unit cell (as well as the average angle) increases. Similar behavior is seen in LCO single polycrystals. A large thermal expansion appears, starting at T $\approx$ 30K with a peak at around T = 50K.[64] In the single ion approximation, HS Co3+ state has a larger radius ($\approx 0.61\mathring{A}$) than the LS state ($\approx 0.545\mathring{A}$).[65] According to the band model, hybridization of d and p orbitals would naturally straiten the angle (the p-p angle is 180°), rotating the octahedra and increasing the size of the unit cell. The molar heat capacity behaves similarly; it remains constant up to $\approx$ 40K, then rises steadily with increasing T. [66] To my knowledge it has never been fitted to a power law.

Thermal conductivity measurements demonstrate the same steady behaviour until about 40K, and then a dip with a minimum at about 150K.[31] This fits well with the molar heat capacity and lattice expansion measurements, with thermal conductivity favoring p-d hybridized type bonds.

Measurements on bulk LCO confirm the presence of the magnetic moment;[47, 1] it is weak but present as seen in Fig. 1.1. Because long range magnetic order in $LaCoO_3$ doesn't exist, how can that be? Measurements by Asai et. al.[67] show a broad "ferromagnetic" peak. Scattering (1.07 0 0), indicates a presence of short range "ferromagnetic" correlations.

According to NEXAFS study,[68] the spectral shape of strained LCO film (grown on 1.0% Nb doped $SrTiO_3$) taken at 20K is well described by 64% Co3+ LS and 36% Co3+ HS mixture, but Co $L_{2,3}$ SXMCD measurement shows a deficiency of HS Co3+ spins. According to authors, this implies the existence of non-homogeneous distribution of HS spins, creating spin clusters in LCO.[68] This fits well both with measurements by Asai et al. as well as our claim that magnetic moment originates on twinning interfaces. They would naturally appear cluster like on spectral images.

Magnetic force microscopy (MFM) measurements were done on LCO grown on a $SrTiO_3$ substrate (positive strain) and $LaAlO_3$ substrate (negative strain). For LCO grown on $LaAlO_3$, scans at 0.1T field reveal no magnetic structure, but scans of LCO on $SrTiO_3$ reveal the presence of sharp magnetic domains that disappear

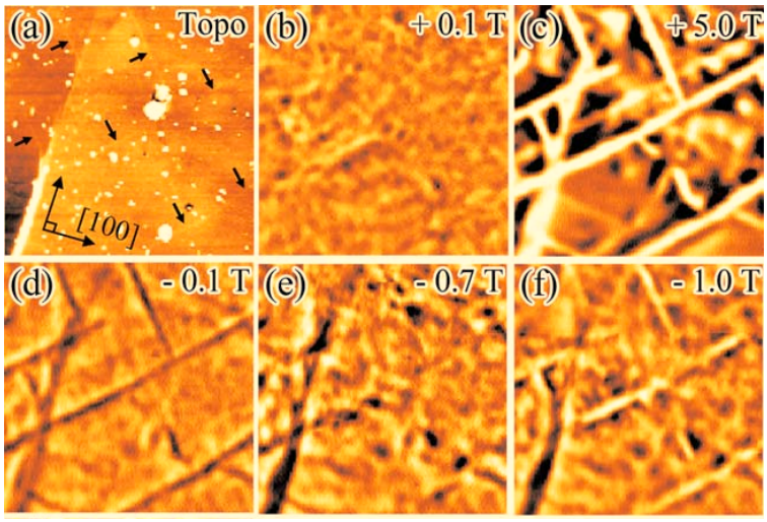

Figure 1.14: MFM images of 3 × 3 μ^2 LCO/STO film taken during an isothermal magnetic field sweep at T = 10 K after ZFC. The image on the upper left has a small insert depicting pseudocubic vector orientation. A magnetic fault line perpendicular to [1 0 0] direction is visible on the left side in panels c, d, e, f. This could be one of the (1 0 0) twinning interfaces. Figure taken from Ref.[16]

at T ≈ 100K.[16] The authors interpret the scan to show wide magnetic domains, with lines indicating transition regions. We see it differently. It is known that pure LCO crystals undergo twinning.[34, 5, 35] Similar twinning exists for strained films. A certain volume fraction of a strained LCO on $SrTiO_3$ would exist in the so called pseudomorphic state, the rest of the film away from the substrate would be in a twinned state.[35] The twinned part is similar to the bulk LCO and it is possible that twinning interfaces exist in it. The MFM contrast on the Fig. 1.14 (frequency shift $\Delta f \propto \partial_z F_z = m_z \partial_z^2 B_z$) are not magnetic fields, but second derivatives of fields. What we could be seeing in Fig 1.14 are not magnetic domains separated by non-magnetic transition lines, as authors claim,[16] but instead the lines indicate the magnetic moments of the twinning interfaces viewed edge on separated by wide non-magnetic regions. The thickness of the edge of the twinning interface is less then 3 nm, while the lines on the image appear to be 100nm or more, but that is due to the low resolution of MFM apparatus.

1.0.8 Introduction Summary

There is no evidence of a significant effect of oxygen doping on the surface or impurity contribution to the magnetic moment in LCO. Since there is no JT distortion detected, oxygen octahedra do not deform and no mechanism exists that would enable ferromagnetic interactions in LCO in the bulk. The only interactions possible are antiferromagnetic. The strength of antiferromagnetic interactions is controlled by the Co-O-Co angle. No evidence of long range antiferromagnetic order exists, but net magnetic moments exists in nanoparticles, strained planes and on (we claim) twinning planes in the bulk. What is the mechanism to produce a moment at all and how can antiferromagnetic interactions alone produce what appears to be a ferromagnetic moment? In the rest of this thesis, we will attempt to model interactions on the twin interfaces with a mean-field calculation and demonstrate how a break in the homogeneous distribution of 163° Co-O-Co bonds with an alternating patterns of 161° and 165° angle bonds creating a net magnetic moment on the twinning interfaces in bulk polycrystals. We believe the same mechanism could be responsible for magnetic interactions in nano-particles and LCO grown on positive strain substrate.

Chapter 2

Neutron Scattering

It has been a common claim that there is no magnetic moment in the bulk LCO and that all measurements of the moment were either due to surface doping by oxygen atoms[58] or impurity contributions in nanoparticles.[59] In a single polycrystal of LCO, both the surface effects and impurity concentrations are negligible. Magnetic susceptibility measurements have been done on an LCO polycrystal,[1] confirming the presence of a net moment in the bulk. That is not enough. Susceptibility measurements cannot determine the type of ordering present (whether it is ferromagnetic or chiral for example). Paramagnetic behaviour can also be mistaken for a weak ferromagnetic moment.

Another way to measure the moment is by polarized neutron scattering. Neutron magnetic moment couples to electron moments inside the material. This effect can be exploited to detect the magnetic structure inside the sample crystal (if any). A neutron incident on a crystal will undergo diffraction inside an ordered crystalline material. A monochromatic beam of neutrons will create a diffraction pattern corresponding to the crystal structure(see Fig. 2.4 and Fig. 2.5). Scattering can occur from both magnetic moments on the ion (magnetic scattering) as well as nuclei (nuclear scattering). If an unpolarized neutron beam is scattered from a crystalline lattice, the nuclear scattering contribution will obscure significantly weaker magnetic scattering.

There is a way around that. To eliminate the effect of nuclear scattering, polarized neutron scattering is used. This type of experiment is shown in Fig. 2.2. A beam on

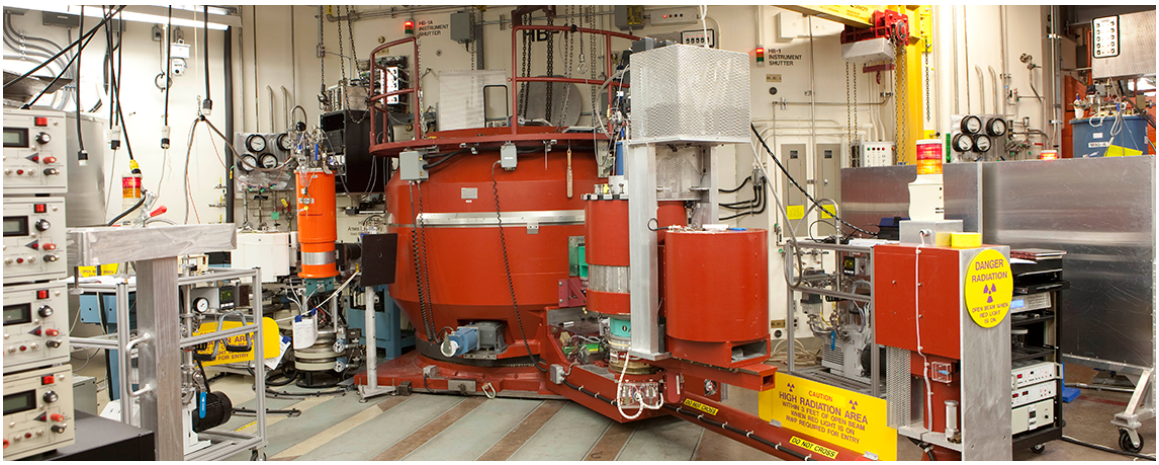

Figure 2.1: HB-1 PTAX instrument that was used for the neutron scattering measurements in Fig. 2.6. It is designed for polarized beam measurements, with high flux and wide neutron energy spectrum (5meV - 120meV), making this instrument optimal to study magnetic behaviour in solid materials. The instrument is designed to fit all available sample environment equipments, including a He^4/He^3 dilution refrigerator, standard He^4 flow cryostats, a 4He cryofurnace, and a variety of closed-cycle refrigerators[17] The geometry of this instrument is well suited for investigation of small samples and weak scattering. Figure taken from Ref. [17]

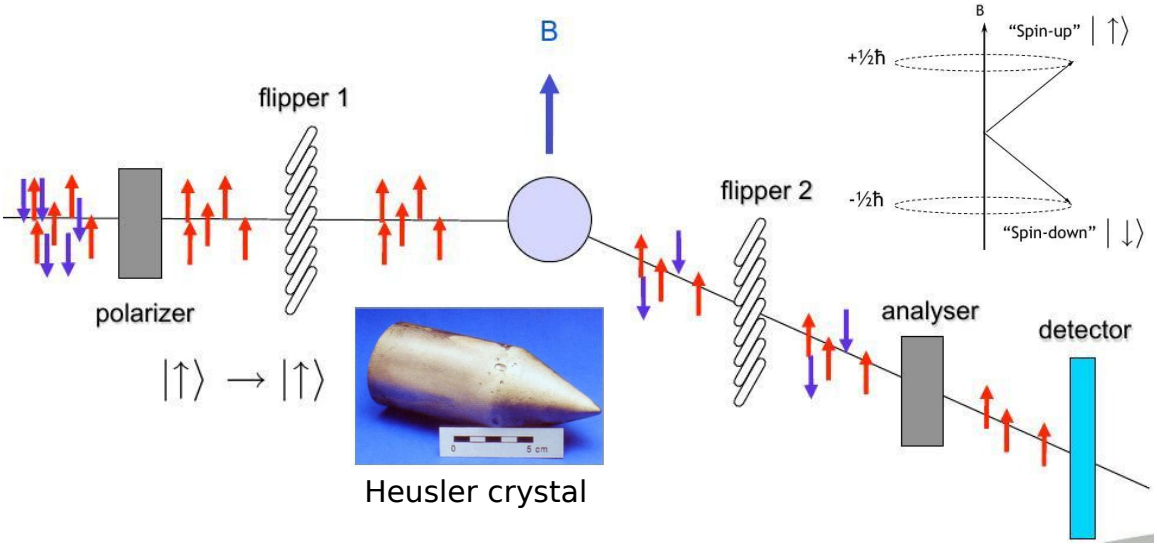

Figure 2.2: A uniaxial polarization analysis experiment. A beam of neutrons is aligned with Heusler crystals, then sent through the sample. The number of spin flipped neutrons (N_+) and the number of non spin flipped neutrons (N_-) is measured. Image taken from Ref. [18]

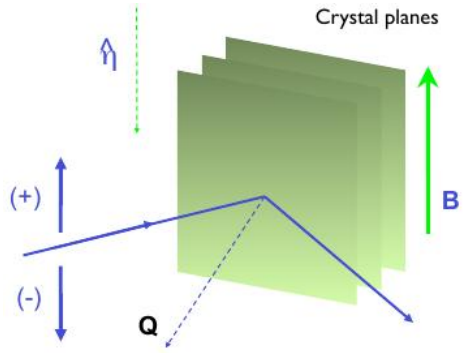

Figure 2.3: Heusler crystals. Polarization vector of the outgoing neutrons in a beam is in the same direction as the magnetic field. Flipping ratio was 9.8 in our experiment. Image taken from Ref. [18]

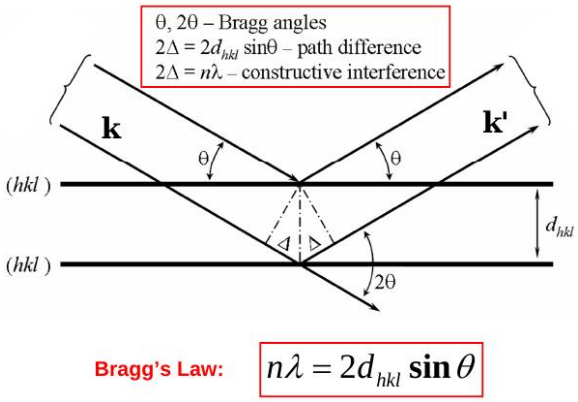

Figure 2.4: Bragg scattering from a plane. Points only appear for constructive interference at $n\lambda = 2d_{hkl}\sin\theta$

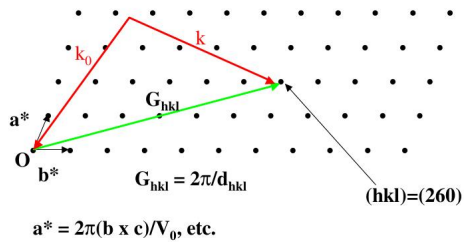

Figure 2.5: Bragg scattering points. Lattice vectors are: a, b, c and reciprocal lattice vectors are a*, b*. Miller indices are h, k, l.

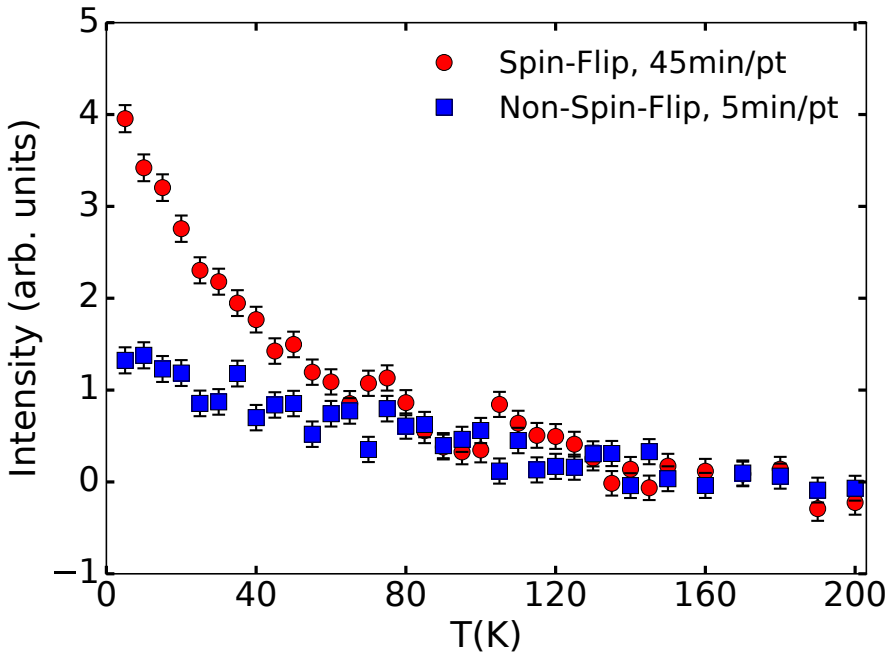

Figure 2.6: Polarized neutron intensity of the (1 0 0) pseudocubic Bragg scattering vs T for both the spin-flip and non-spin-flip configurations with the background subtracted as described in the main text.

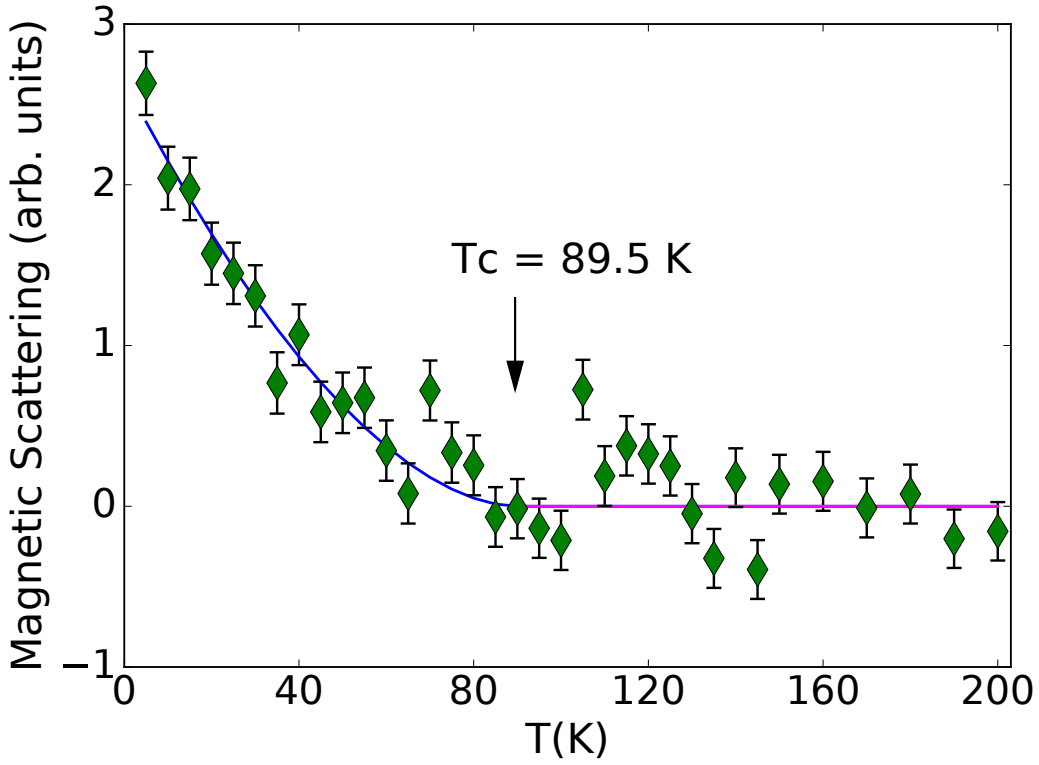

Figure 2.7: The difference between background subtracted spin-flip and non-spin-flip intensities vs T, where non-spin-flip intensity is normalized by the flipping ratio of 9.8. The curve represents Eq. 2.6 with $T_C = 89.5$ K, $A = 2.65$, $\beta = 0.88$, $B = 0$ and $C = 0$.

polarized neutrons is incident upon a crystalline material. A weak magnetic guide field is applied to the sample in the same direction as the neutron polarization vector **P**. A neutron incident upon a magnetic site in the sample can undergo spin flip. Measuring the number of just the spin-flipped neutrons enables the experimenter to see the effects of magnetic scattering, eliminating the effects of nuclear scattering.

Our polarized neutron scattering experiments were performed on a LCO single polycrystal using the triple axis spectrometer HB1 at the High Flux Isotope Reactor, shown in Fig. 2.1, with a collimation configuration of 48', 80', 80', and 240'. The last four numbers represent alignment of the neutron beam in minutes for pre-monochromator, monochromator-sample, sample-analyser and analyser-detector. In our experiment, the neutron beam was polarized with the use of Heusler crystals (see Fig. 2.3). The Bragg reflection intensity for the crystals is given by

$$\frac{d\sigma}{d\Omega} = F_N^2(\mathbf{Q}) + 2F_N(\mathbf{Q})F_M(\mathbf{Q})\big(\mathbf{P}\cdot\hat{\boldsymbol{\eta}}\big) + F_M^2(\mathbf{Q}), \tag{2.1}$$

where $\mathrm{F}_{N,M}$ are the nuclear and magnetic structure factors and $\hat{\boldsymbol{\eta}}$ is the direction of the magnetic moment of the Heusler crystals, **P** is the polarization direction of the neutrons in the beam. For $\mathbf{P}\cdot\hat{\boldsymbol{\eta}}$ = -1,

$$\frac{d\sigma}{d\Omega} = \Big[F_N(\mathbf{Q}) - F_M(\mathbf{Q})\Big]^2, \tag{2.2}$$

and for $\mathbf{P}\cdot\hat{\boldsymbol{\eta}} = 1$,

$$\frac{d\sigma}{d\Omega} = \Big[F_N(\mathbf{Q}) + F_M(\mathbf{Q})\Big]^2. \tag{2.3}$$

For the case of $\mathrm{F}_N(\mathbf{Q}) = \mathrm{F}_M(\mathbf{Q})$ neutron scattering with the antiparallel polarization to the Heusler crystals $\mathbf{P}\cdot\hat{\boldsymbol{\eta}}$ = -1, will be suppressed and the reflected beam will be effectively polarized.

The polarizing efficiency P_f is

$$P_f = \frac{2F_N(\mathbf{Q})F_M(\mathbf{Q})}{F_N(\mathbf{Q})^2 + F_M(\mathbf{Q})^2}. \tag{2.4}$$

Since the polarization efficiency $P_f \neq 1$, it is important to know the flipping ratio $F = N_-/N_+$ (here N_- and N_+ are neutrons polarized parallel and antiparallel with respect to $\boldsymbol{\eta}$). In our case, flipping ratio of 9.8 was achieved with an incident neutron

energy of 13.5 meV. A neutron encountering a magnetic moment inside the sample can be spin-flipped. Spin-flip(SF) and non-spin-flip (NSF) intensities were measured with the neutron spin aligned along Q. The background contribution had to be eliminated, using

$$SF_a = \frac{F-1}{F+1} SF_m, \tag{2.5}$$

where subscript 'a' stands for 'actual' and 'm' stands for 'measured'. For the LCO crystal, the first nuclear Bragg scattering point is (1 0 0) in the reciprocal pseudocubic coordinates. Looking at just the SF_a neutrons, we saw a sharp peak. This demonstrates a net moment in the crystal. A paramagnetic moment would have produced a shallow, broad peak at (1 0 0). A chiral moment would have produced satellite peaks around (1 0 0). As we will claim in the later parts of this thesis (see section 5), twinning interfaces produce not a ferromagnetic but a net moment. Had we checked Bragg scattering point (1/2 0 0) we might have seen another sharp peak, verifying the existence of an anitferromagnetically ordered moment. A closed-cycle refrigerator was employed in measuring the T dependence of the magnetic and nuclear reflections for $4 < T < 300$ K. Measurements were done at the (1 0 0) point. The field at the sample was 16 to 18 Oe throughout the experiment and all data were therefore taken under FC conditions. The $LaCoO_3$ single crystal was grown by the floating zone technique using an optical image furnace as reported elsewhere.[1] One piece of the crystal of about 4 mm in diameter and 8 mm in length was used for the neutron diffraction study. Figure 2.6 shows data collected in both the spin-flip and non-spin-flip configurations. The no-spin-flip intensity is divided by the flipping ratio. A background contribution, determined by averaging the data for $145 < T < 200$ K, is subtracted from each data set. The spin-flip configuration clearly shows a small, but significant magnetic Bragg scattering contribution. The difference of the two sets of data is plotted in Fig. 2.7. Using the difference, we can characterize the critical behavior associated with the phase transition to long-range order by fitting to

$$I = At^{2\beta} + B + Ct, \tag{2.6}$$

where $t = (T_C - T)/T_C)$ and A is nonzero only for $t > 0$. T_C is set to 89.5 K,

the value obtained in magnetization experiments.[29] A fit with $B = 0$ and $C = 0$ yields $A = 2.66 \pm 0.21$ and $\beta = 0.88 \pm 0.12$. The error estimates reflect only the statistical error of the fit. The critical exponent β is fairly consistent with the result from magnetization measurements[53, 29] on bulk LCO particles, $\beta = 0.63 \pm 0.02$. Including a linear background term in the fit yields $A = 2.64 \pm 0.23$, $\beta = 0.88 \pm 0.12$, and $C = -0.01 \pm 0.09$. If, instead, a T-dependent term, BT, is included, we obtain $A = 2.64 \pm 0.22$, $\beta = 0.97 \pm 0.14$, and $B = 0.07 \pm 0.05$. Neither of the latter two fits improves the quality of the fit significantly over the one with $B = 0$ and $C = 0$.

The value of β from the fits is clearly larger than the mean-field value $1/2$, which is larger than the order parameter for bulk two or three dimensional phase transitions. The experimental value for LCO is, however, consistent with models of bulk-assisted surface ordering $\beta = 0.75$ [29, 69] in which the surface orders with different critical behavior from the bulk. Two differences between LCO and the surface-ordering models are that bulk LCO does not order sufficiently far from surfaces and we observe a net moment, which might seem inconsistent with the antiferromagnetic order parameter of the bulk. However, antiferromagnetic moments away from the surfaces are close to ordering while those near the surface do order, [29] and we will argue that, despite the net moment being generated, the ordering is essentially antiferromagnetic.

Chapter 3

Geometric model

The behavior of LCO magnetism well away from twin interfaces and other defects has been fairly well characterized. Experiments [53, 29, 59, 70] and calculations [14] indicate that antiferromagnetic correlations are supported only for γ greater than the critical value $\gamma_C \approx 163°$. The uniqueness of bulk LCO magnetism derives from the average value of γ decreasing with T to γ_C at T_o. The magnetic structure at twin boundaries is more complicated than that of the bulk far from the interface and can lead to antiferromagnetic ordering with a net moment along H_z. We first show how the interface can lead to a magnetic bond structure that is asymmetric with respect to the two antiferromagnetic sublattices.

The most common LCO twin interface in LCO is at a (1 0 0) pseudocubic plane. [35, 5] Although other twin representations are possible, they are relatively uncommon, so we use the (1 0 0) one to model the possible consequences of a twin plane in LCO. A (1 0 0) plane can be visualized in the unit cell shown in Fig. 3.1 as a plane containing the central La ion, four other La ions, and no Co ions. There are four unique crystallite orientations possible associated with mirror reflections about the three possible (1 0 0) planes. Although the oxygen atomic positions are not distorted on the twin plane itself, the crystalline planes on either side are slightly misaligned with respect to each other. In our model, we locate the twin interface on an oxygen plane because that allows the oxygen octahedra to remain undistorted; only the angles between them change. The misalignment of crystal structures on either side of a

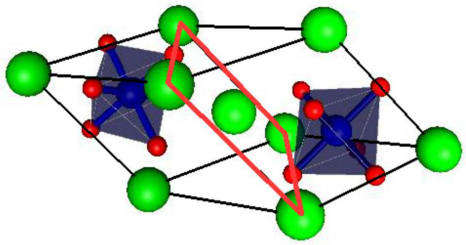

Figure 3.1: The primitive rhombohedral LCO cell showing La ions (green) at the center and corners and two Co ions (blue) along with their oxygen octahedra. The rhombohedron is elongated along the line containing the two Co ions. The red lines connecting four La ions represents one of three possible twinning planes in the pseudocubic representation, each one containing four La ions at the rhombohedron corners and the central La ion, but no Co ions.

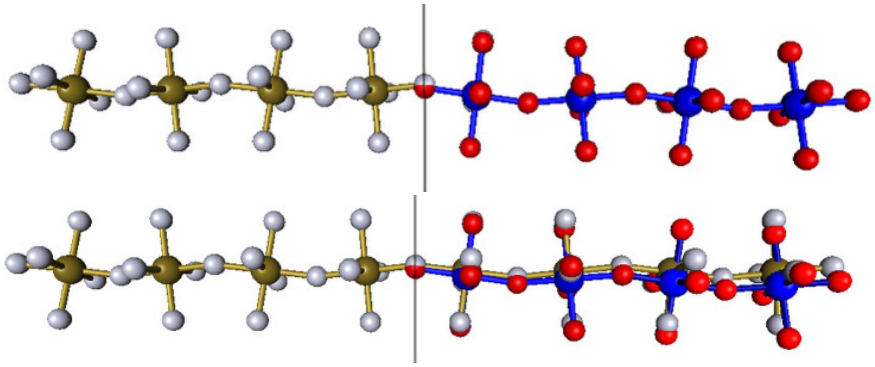

Figure 3.2: A chain of Co ions crossing a twin interface, represented by the vertical line at the center. The upper figure shows blue ions representing a chain of Co ions that is nearly perpendicular to the twin plane in a crystallite to the right of the twin plane. Each Co is surrounded by its oxygen octahedron (red). The gold-colored Co ions, surrounded by their oxygen octahedra (white), are from the crystallite to the left of the twin interface. The bi-colored oxygen is on the twin interface and is shared by both chains. The lower figure is the same as the upper one except that the chain from the left is extended into the right crystallite to emphasize the small misalignment of the two chains. The Co-O-Co angles are near 163° except across the twin interface, where half the bond angles are near 165° and half near 161°, in an alternating pattern. The Co-O-Co angle at the twinning connection is 165° for the chain shown here. All other Co-O-Co angles are 163° on the chain.

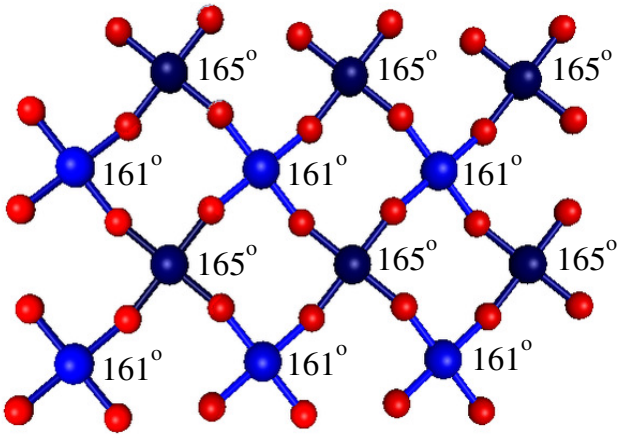

Figure 3.3: The pattern of ions in one plane adjacent to the twin interface with strongly antiferromagnetic bonds across the interface (dark) alternating ions with non-magnetic bonds (light) across the interface. The angles associated with the bonds across the interface (perpendicular to the page, but not shown) are next to the associated Co ions. All bond angles in the plane shown are 163°, as are all other angles for bonds that do not traverse the twin interface.

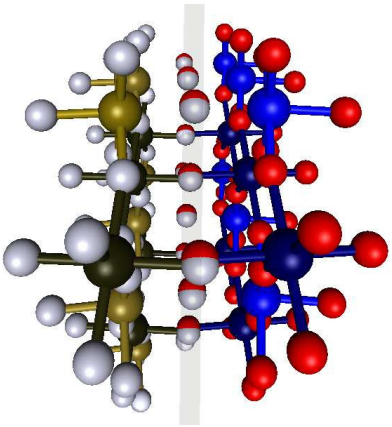

Figure 3.4: A side view of the twin interface where only the strong antiferromagnetic bonds are shown spanning the interface (shown in the shaded region). The non-magnetic bonds are not shown. The La ions are also not shown for clarity, including those that lie on the twin boundary. The two planes of Co ions are parallel. The bi-colored oxygens are on the twin interface and are shared by oxygen octahedra from each of the two twin domains.

twin plane is illustrated in Fig. 3.2, where, in the upper figure, a chain of Co ions in each of the crystals is shown nearly perpendicular to the twin interface located at the center where the bi-colored oxygen is shared by both chains. In the lower figure, the chain of crystal on the left is extended into the crystal on the right to illustrate the misalignment. An important consequence of the misalignment is that the Co-O-Co bonds across the twin plane deviate from angles near the critical angle $\gamma_C \approx 163^\circ$ that exist for all other bonds. Half the bonds spanning the twin interface have $\gamma \approx 165^\circ$ and are adjacent to the other half that have $\gamma \approx 161^\circ$.

Based on studies of LCO nanoparticles [29] and thin films, [61, 28, 35, 71**?**] bond angles with $\gamma \approx 165^\circ$ should be strongly magnetic, much more so than in bulk LCO, whereas $\gamma \approx 161^\circ$ would result in essentially non-magnetic bonds[14, 53, 70]. First principles generalized gradient approximation (GGA) and local density approximation (LDA) [14] suggest the same dependence of the magnetization on γ; greater rhombohedral distortions corresponds to smaller values for γ and that suppresses the magnetic moment. The alternating pattern of strongly magnetic and non-magnetic bonds across the twin interface is depicted in Fig. 3.3, which shows the Co and O ions in one plane adjacent to the twin interface and Fig. 3.4, which shows the bonds across the interface. The alternating configuration of bond strengths will affect the two antiferromagnetic sublattices asymmetrically. All Co-O-Co bonds not spanning the twin interface remain near the normal bulk angles close to 163°, with correspondingly weak antiferromagnetic interactions that are insufficient to cause long-range order on their own. In the actual LCO system, the distortions could propagate further than one Co plane from the twin interface, but that would likely not alter the physical behavior qualitatively.

Chapter 4

Ground State Calculation

To explore the magnetic consequences of the pattern of alternating strongly antiferromagnetic and non-magnetic bonds, we approximate the system by interacting classical local moments located at each Co ion site in the two planes adjacent to the twin interface.

The strong magnetic interactions of strength J across the interface alternate with bonds of zero strength, as shown in Fig. 3.3 and 3.4. The moments away from the interface, which do not order in LCO but still contribute to the ordering at the twin interface, are represented in the model by an effective interaction j between all Co ions within each Co plane. Note that $J > j$ in our model because a stronger magnetic interaction is expected for the larger Co-O-Co bond angle [53, 14]. In the ground

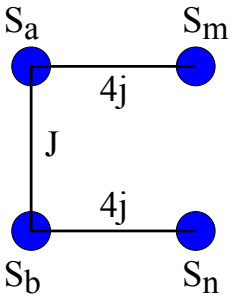

Figure 4.1: Mean-field exchange interactions. S_a and S_m are on one side of the twin interface and S_b and S_n are on the other. The S_a and S_m each have four neighbours, each with interaction strength j. S_a and S_b interact with strength J and S_m and S_n do not directly interact with each other.

state calculations, each of the four kinds of spin, S_a, S_b, S_m and S_n, behave like the others of the same kind. Hence, the magnetic exchange interaction structure of this simple model is shown in Fig. 4.1 and is represented by a simplified magnetic model Hamiltonian with a magnetic field of strength H_z in the z direction,

$$\begin{aligned}\mathcal{H} &= 4j\overrightarrow{S_a}\cdot\overrightarrow{S_m} + 4j\overrightarrow{S_b}\cdot\overrightarrow{S_n} + J\overrightarrow{S_a}\cdot\overrightarrow{S_b} \\ &\quad -H_z\Big(S_{az} + S_{bz} + S_{mz} + S_{nz}\Big) \\ &\quad +F\Big(\sum_{i\in x,y,z}\Big[S_{a,i}^4 + S_{b,i}^4 + S_{m,i}^4 + S_{n,i}^4\Big]\Big). \end{aligned} \tag{4.1}$$

The magnitude of each moment is constrained by $|S_i| = 1$ for $i \in a, b, m, n$. The S_a and S_b spins interact with magnitude J across the interface, and there are four interactions of strength j between S_a and S_m in the plane on one side of the interface and, likewise, four between S_b and S_n in the plane on the other side of the interface, as shown in Fig. 4.1. There are no direct interactions between S_m and S_n or between spins in the two planes and spins further from the interface. Local moments on each cobalt site also interact with the oxygens in the corners of the octahedra. To model this behavior, we introduce a cubic anisotropy into the model of strength F. Moments are attracted to the corners of the octahedra for $F < 0$ and repelled for $F > 0$. Similar models with quartic terms in the Hamiltonian were investigated previously by other groups [19, 20, 72]

We investigate the ground state by minimizing the energy represented by the Hamiltonian. Details of the procedure are described in the appendix. We tested it on a simple Heisenberg model with uniaxial exchange anisotropy and cubic anisotropy represented by

$$\begin{aligned}\mathcal{H} &= 4j\Big[\Delta\Big(S_{a,x}S_{m,x} + S_{a,y}S_{m,y}\Big) + S_{a,z}S_{m,z}\Big] \\ &\quad -H_z\Big(S_{az} + S_{mz}\Big) \\ &\quad +F\sum_{i\in x,y,z}\Big[S_{a,i}^4 + S_{m,i}^4\Big], \end{aligned} \tag{4.2}$$

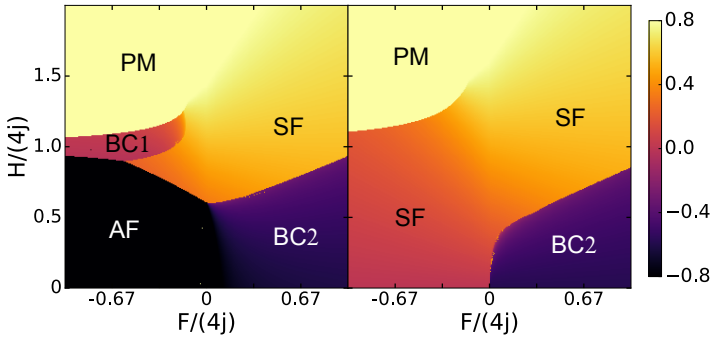

Figure 4.2: The ground state maps for $J = 0$, with $\Delta = 0.8$ (left) and 1.0 (right). The case $\Delta = 0.8$ agrees well with previous studies [19, 20] and the case $\Delta = 1.0$ is isotropic, as in the model developed for the LCO twin interface. For $\Delta = 0.8$, both the antiferromagnetic (AF) state with moments along H and the biconical states (BC1 and BC2) are clearly visible, as is the paramagnetic (PM) state that appears at high fields. For $\Delta = 1.0$, the antiferromagnetic state is absent, as is expected.

where $\Delta < 1$ represents uniaxial anisotropy. The left panel of Fig. 4.2 shows our simulation results with $\Delta = 0.8$ for the net moment along H_z as a function of H_z and F. Such a model has been studied previously, [19, 20] and the results are essentially the same as ours; the only significant difference is that the boundary between the biconical BC2 and paramagnetic (PM) phases is flatter in the previous simulations. The antiferromagnetic state is visible for low H and $F < 0$. Higher fields result in the formation of a biconical state, BC1, [19, 20] in which one spin points towards the corner of the oxygen octahedron in the direction of H_z, and the other spin remains near the x-y plane, pointing towards one of octahedral corners. The angle between the spins is close to 90°. As the magnitude of H_z increases, the system becomes paramagnetic. For $F > 0$ and small H_z, a biconical BC2 state occurs as spins avoid the octahedral corners and instead tend to point towards the octahedral diagonals.

The right panel of Fig. 4.2 shows results for $\Delta = 1$, which represents isotropic exchange interactions and corresponds to the model in Eq. 4.1 for $J = 0$, which creates two identical noninteracting planes, only one of which is shown in the figure. For $F < 0$ and small H_z, the ground state is a spin-flop configuration (SF) with the moments aligned mostly perpendicular to the applied field with a small component

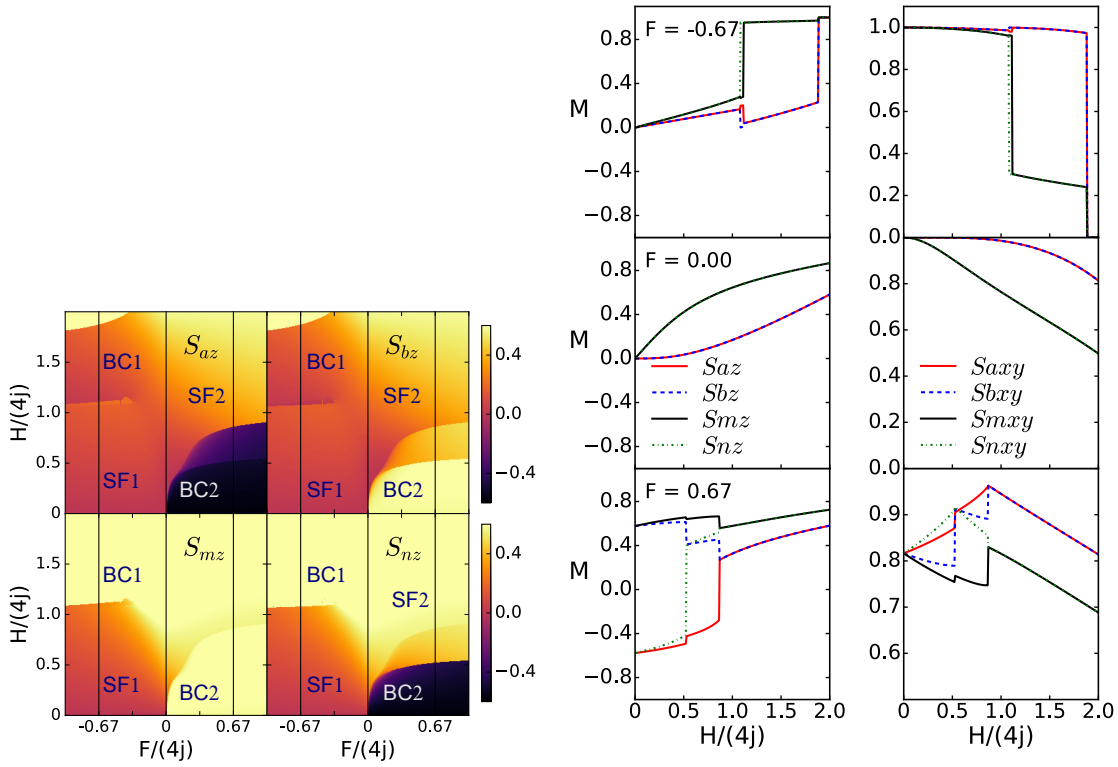

Figure 4.3: The ground state configuration for $J/(4j) = 2/3$ for the moments along H applied in the z direction for the four types of spin as a function of H and F (upper figure) calculated by minimizing the energy in Eq. 4.1 and the moments of each component parallel (left) and perpendicular (right) of the spins as a function of H along cuts at $F/(4j) = -0.67$, 0 and 0.67 (lower figure). Biconical states (BC) similar to those in Fig. 4.2 are observed as well as an intermediate state between the biconical state and the paramagnetic state for $F > 0$.

induced along the field. For larger fields, the system becomes paramagnetic with a significant moment along H_z. For $F > 0$, the low field biconical BC2 state is observed. It gives way to a spin-flop state (SF) at higher fields. In our case BC1 and BC2 states are different from Selke (see Fig. 4.6).

The mean-field calculations ignore fluctuations. However, for $\Delta = 1$, density matrix renormalization group (DMRG) calculations in 1D, [72] for which fluctuations are maximized, yield results qualitatively similar to those of the analogous mean-field calculations.

Simulations with $J \neq 0$ were done as well. Fig. 4.3 shows the ground state diagram

for Eq. 4.1 with $j = 15$ and $J/(4j) = 2/3$. We use the value $J/(4j) = 2/3$ throughout this discussion, but the results were found to be qualitatively similar for simulations with $J/(4j) = 1/3$ and $4/3$. For $F \leq 0$, the ground state is a SF configuration with the moments predominantly perpendicular to H_z with small components along H_z. This can be seen in Fig. 4.3, which shows cuts of the grounds state diagram at $F/(4j) = -0.67$, 0, 0.67. In the lower part of Fig. 4.3, the moments on the left are along the field and those on the right are perpendicular to the field; for example, the label $Saxy$ signifies the total perpendicular moment $\sqrt{S_{ax}^2 + S_{ay}^2}$. (The same notation is used for Fig. 4.4 and 4.5. For $F > 0$, a biconical BC2 state is observed at small H, as shown in Fig. 4.3. As H_z increases, the system evolves towards SF, with an intermediate phase separating the two. The nature of BC1 and BC2 state can be seen from the the cuts at $F/(4j) = -0.67$, 0 and 0.67. The BC1 state visible for $F < 0$ and the BC2 state is visible for $F > 0$.

Although there is no compelling model where $\gamma = 165^\circ$ corresponds to a dominant ferromagnetic interaction between S_a and S_b, we investigated the consequences of $J < 0$ in the mean-field approximation. Figure 4.4 shows the ground state diagram for $J/(4j) = -2/3$ and cuts at $F/(4j) = -0.67$, $F = 0$ and $F = 0.67$. For $F \leq 0$, the ground state is a SF configuration with the moments predominantly perpendicular with a small component along the field. The main difference between this case and that of $J/(4j) = 2/3$ is the orientation of S_a and S_b spins, which now always align in the same direction. For $F < 0$, the BC1 state is absent and the SF state transitions directly into the PM state with increasing H. This is expected because the interaction between S_a and S_b is ferromagnetic. For $F > 0$ a biconical BC2 state remains. It differs from the case for $J < 0$ in that the two moments S_a and S_b are aligned in the same direction, as are the two moments S_m and S_n.

Finally, we introduce the tilt of the octahedron into the simulation. As shown in Fig. 3.2, 3.3, and 3.4, each octahedron is tilted 165° relative to its neighbors, in an alternating pattern. The transformation matrix that rotates the spins :

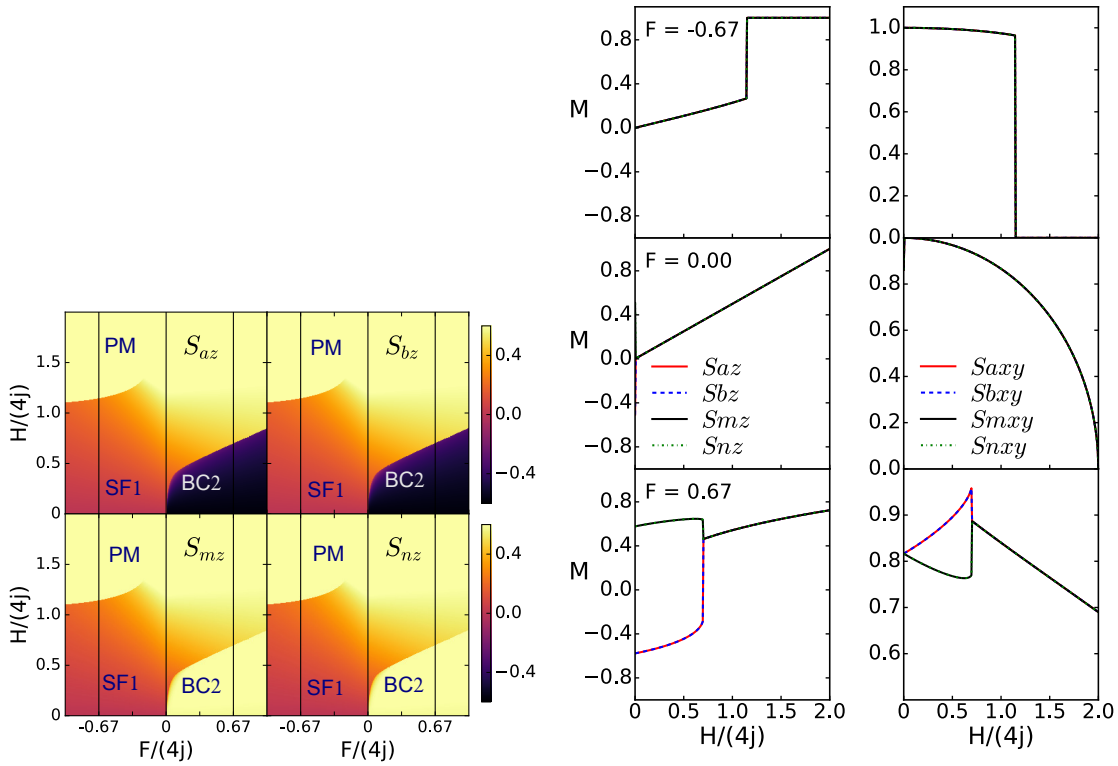

Figure 4.4: The ground state configuration for $J/(4j) = -2/3$ for the moments along H applied in the z direction for the four types of spin as a function of H and F (upper figure) calculated by minimizing the energy in Eq. 4.1 and the moments of each component parallel (left) and perpendicular (right) of the spins as a function of H along cuts at $F/(4j) = -0.67$, 0 and -0.67 (lower figure). A biconical state (BC) is observed for $F > 0$.

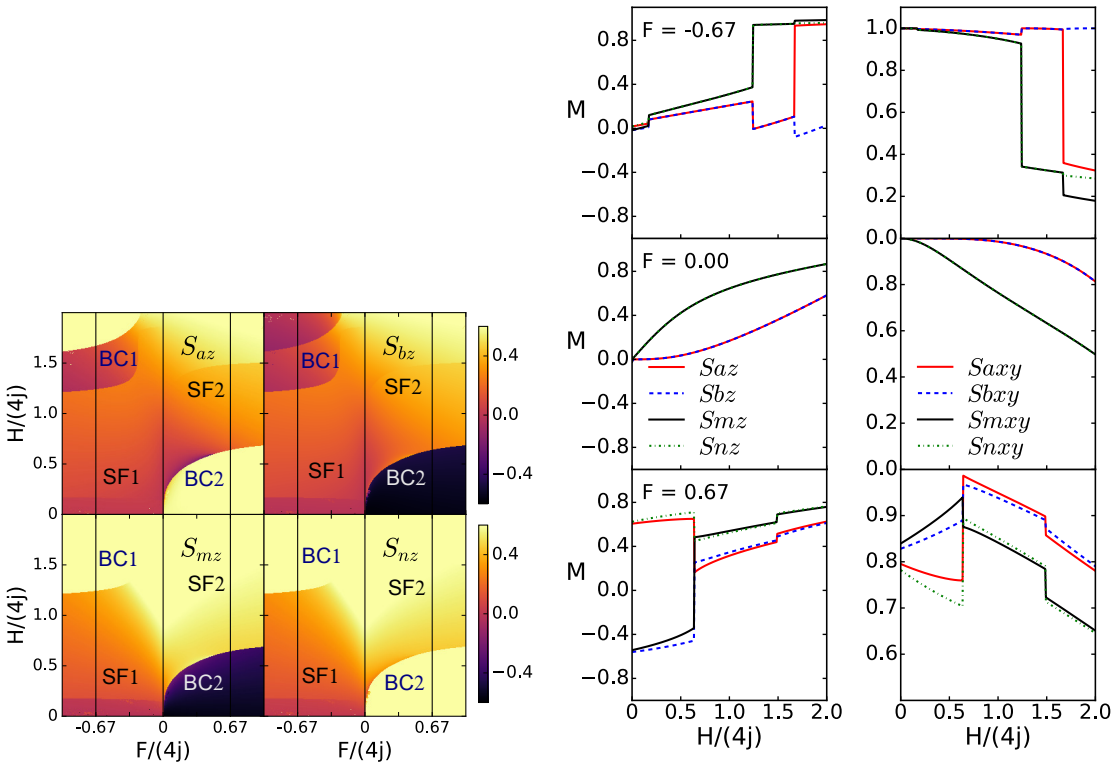

Figure 4.5: The ground state configuration with $J = J/(4j) = 2/3$, similar to that shown in Fig. 4.3 except that the oxygen octahedra are tilted with respect to z in an alternating pattern as described in the text. A biconical-like (BC) state is observed for both F > 0 and F < 0.

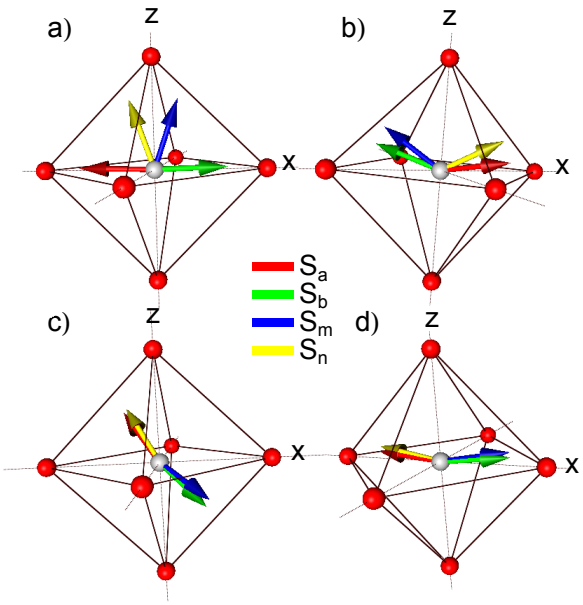

Figure 4.6: Spin orientation inside the oxygen octahedra. Red spheres are the oxygen atoms, silver is the cobalt atom. The z direction inside the octahedra is tilted by 7.5° with respect to the magnetic field. For F $<$ 0 spins are attracted to the oxygen corners, for F $>$ 0 spins are repelled. The recorded coordinates are for Fig. 4.5. a) BC1 ground state configuration (F/4j = -0.66, H/4j = 1.41). b) Spin flop 1 (SF1) configuration (F/4j = -0.45, H/4j = 0.28). c)BC2 configuration (F/4j = 0.55, H/4j = 0.48). d)Spin flop 2 (SF2) configuration (F/4j = 0.55, H/4j = 0.78).

$$\mathbf{M_1}^{-1}(\alpha_0) = R_y(\alpha_0) \cdot R_z(\alpha_0) = \begin{bmatrix} \cos\alpha_0 & \sin\alpha_0 \cos\alpha_0 & \sin\alpha_0 \\ \sin\alpha_0 & \cos\alpha_0 & 0 \\ -\sin\alpha_0 \cos\alpha_0 & \sin^2\alpha_0 & \cos\alpha_0 \end{bmatrix}$$

The second matrix $\mathbf{M_2}$ is similar to $\mathbf{M_1}$, but it also flips the spins into the negative z-direction and rotates them not in α but $-\alpha$. The ground state is calculated using the modified equation

$$\begin{aligned} \mathcal{H} &= 4j\overrightarrow{S_a} \cdot \overrightarrow{S_m} + 4j\overrightarrow{S_b} \cdot \overrightarrow{S_n} + J\overrightarrow{S_a} \cdot \overrightarrow{S_b} \\ &\quad -H_z\Big(S_{az} + S_{bz} + S_{mz} + S_{nz}\Big) \\ &\quad +F \sum_{i\in x,y,z} \Bigg(\sum_{k\in a,n} \Big[\mathbf{M_1}\overrightarrow{S_k}\Big]_i^4 \Bigg) \\ &\quad +F \sum_{i\in x,y,z} \Bigg(\sum_{k\in b,m} \Big[\mathbf{M_2}\overrightarrow{S_k}\Big]_i^4 \Bigg), \end{aligned} \tag{4.3}$$

where $\mathbf{M_1}$ and $\mathbf{M_2}$ are matrices that rotate spins into the coordinate systems of respective octahedra tilted 7.5° and −7.5° with respect to z. The direction of z is only important when considering the case of tilt and we set it perpendicular to the twin interface.

Some differences are seen in the ground state as a result of the octahedron tilt, as shown in Fig. 4.5. For $F < 0$, the SF state for low fields and the BC1 state at intermediate fields appear qualitatively similar to the case of no tilt in Fig. 4.3, except that, for high H values, instead of a transition from the SF state to the PM state seen in Fig. 4.3, a new BC1-like state exists between the SF and PM states with S_a and S_b nearly perpendicular to each other and with S_m and S_n nearly parallel. For $F > 0$, the tilt and no tilt ground states appear superficially similar, but the transition between PM and BC2 states are separated by an intermediate state as F increases. The transitions become less sharp as F decreases towards zero. The position of the spins in tilted octahedra under the influence of the magnetic field is seen in Fig. 4.6; BC1 and BC2 states are similar to those investigated by Bannasch et al.[19], but four interacting spins instead of two create a slightly different picture.

Chapter 5

Mean Field theory

To study the model for $T > 0$, we employed the mean-field approximation

$$\mathcal{H} = \sum_{k \in a,b,m,n} \overrightarrow{S_k} \cdot \overrightarrow{H}_{MF,k}, \tag{5.1}$$

with the effective mean fields

$$\begin{aligned}
\overrightarrow{H}_{MF,a} &= 4j\overrightarrow{\langle S_m \rangle} + J\overrightarrow{\langle S_b \rangle} + \overrightarrow{H} + F\overrightarrow{C}_a \\
\overrightarrow{H}_{MF,b} &= 4j\overrightarrow{\langle S_n \rangle} + J\overrightarrow{\langle S_a \rangle} + \overrightarrow{H} + F\overrightarrow{C}_b \\
\overrightarrow{H}_{MF,m} &= 4j\overrightarrow{\langle S_m \rangle} + \overrightarrow{H} + F\overrightarrow{C}_m \\
\overrightarrow{H}_{MF,n} &= 4j\overrightarrow{\langle S_b \rangle} + \overrightarrow{H} + F\overrightarrow{C}_n,
\end{aligned} \tag{5.2}$$

and the four terms $\overrightarrow{C}_p$ are given below. The exchange parameters j and J are those introduced earlier and summarized in Fig. 4.1. The symbol $\odot$ represents the Hadamard vector product; it is a piece-wise multiplication of x, y, and z components yielding components such as $(S_{ax})^3$, $(S_{ay})^3$, $(S_{az})^3$ in the x, y, and z directions, respectively. To simulate the effect of crystal field within the octahedra, the spins are rotated into the coordinate system of the octahedra to interact with the field, then rotated back into the xyz coordinates. This is accomplished by $\mathbf{M}_{1,2}$ matrices. Four terms $\overrightarrow{C}_p$ are given below

$$
\begin{aligned}
\overrightarrow{C}_a &= \mathbf{M}_1^{-1}\left[\left(\mathbf{M}_1\overrightarrow{\langle S_a\rangle}\right)\odot\left(\mathbf{M}_1\overrightarrow{\langle S_a\rangle}\right)\odot\left(\mathbf{M}_1\overrightarrow{\langle S_a\rangle}\right)\right] \\
\overrightarrow{C}_b &= \mathbf{M}_2^{-1}\left[\left(\mathbf{M}_2\overrightarrow{\langle S_b\rangle}\right)\odot\left(\mathbf{M}_2\overrightarrow{\langle S_b\rangle}\right)\odot\left(\mathbf{M}_2\overrightarrow{\langle S_b\rangle}\right)\right] \\
\overrightarrow{C}_m &= \mathbf{M}_2^{-1}\left[\left(\mathbf{M}_2\overrightarrow{\langle S_m\rangle}\right)\odot\left(\mathbf{M}_2\overrightarrow{\langle S_m\rangle}\right)\odot\left(\mathbf{M}_2\overrightarrow{\langle S_m\rangle}\right)\right] \\
\overrightarrow{C}_n &= \mathbf{M}_1^{-1}\left[\left(\mathbf{M}_1\overrightarrow{\langle S_n\rangle}\right)\odot\left(\mathbf{M}_1\overrightarrow{\langle S_n\rangle}\right)\odot\left(\mathbf{M}_1\overrightarrow{\langle S_n\rangle}\right)\right]
\end{aligned}
\tag{5.3}
$$

In the case of non-tilted octahedra, $\alpha = 0$, there is no need change the coordinate system, thus no rotation matrices are necessary.

$$
\overrightarrow{C}_p = \overrightarrow{\langle S_p\rangle}\odot\overrightarrow{\langle S_p\rangle}\odot\overrightarrow{\langle S_p\rangle},
\tag{5.4}
$$

where $p = a$, b, m or n in each term. Each spin $\overrightarrow{S}$ can point in any direction. In order to calculate magnetization, we first write down the partition function Z,

$$
Z = \sum_{i\in a}\sum_{j\in b}\sum_{f\in m}\sum_{d\in n}\exp\left(-\beta\Big[\quad \overrightarrow{H}_{MF,a}\cdot\overrightarrow{S_i} + \overrightarrow{H}_{MF,b}\cdot\overrightarrow{S_j} + \right.
$$
$$
\left. + \overrightarrow{H}_{MF,m}\cdot\overrightarrow{S_f} + \overrightarrow{H}_{MF,n}\cdot\overrightarrow{S_d}\Big]\right)
\tag{5.5}
$$

The $\sum$ is over all possible spin positions. In the limit of infinite spins $N \to \infty$ sum can be replaced by an integral. Normalizing the magnitude of all individual spins to one: $|\overrightarrow{S_i}| = 1$ we are integrating over a unit sphere, partition function for Z_k

$$
Z_k = \int_\alpha\int_\phi \exp\left(-\beta\Big[\quad H_{MF,kx}\sin\alpha_k\cos\phi_k + H_{MF,ky}\sin\alpha_k\sin\phi_k + \right.
$$
$$
\left. + H_{MF,kz}\cos\alpha_k\Big]\right)\sin(\alpha_k)\,\mathrm{d}\alpha_k\,\mathrm{d}\phi_k
\tag{5.6}
$$

with $k = a, b, m, n$. This can be simplified into an integral over a single variable. Using an identity

$$\int_0^{2\pi} e^{x\cos\phi + y\sin\phi} d\phi = 2\pi I_0\left[\sqrt{x^2+y^2}\right], \tag{5.7}$$

where I_0 is a modified Bessel function of the first kind, we can rewrite Z_k as

$$\begin{aligned} Z_k = 2\pi \int_\alpha \quad & I_0\left[-\beta \sin\alpha_k \sqrt{H_{MF,kx}^2 + H_{MF,ky}^2}\right] \\ & \exp\left(-\beta H_{MF,kz}\cos\alpha_k \right) \sin(\alpha_k)\, \mathrm{d}\alpha_k \end{aligned} \tag{5.8}$$

The total partition function $Z_T = Z_a Z_b Z_m Z_n$. Using Helmholtz free energy $F = -T \ln Z_T$, magnetization can be obtained from

$$M = -\frac{\partial F}{\partial H_{MF}}, \tag{5.9}$$

but in our case magnetization is just the sum of four different averaged spins

$$\overrightarrow{M} = N\Big(\overrightarrow{\langle S_a \rangle} + \overrightarrow{\langle S_b \rangle} + \overrightarrow{\langle S_m \rangle} + \overrightarrow{\langle S_n \rangle}\Big) \tag{5.10}$$

so value of each average spin can be obtained by taking the derivative of Helmholtz free energy

$$\langle S_k \rangle_i = \frac{T}{Z_k}\frac{\partial Z_k}{\partial H_{MF,ki}},, \tag{5.11}$$

where $i \in x, y, z$ and $k \in a, b, m, n$. Writing out the derivatives

$$
\begin{aligned}
\langle S_k\rangle_x &= \tfrac{2\pi T}{Z_k}\int_\alpha \; I_1\Big[-\beta\sin\alpha_k\sqrt{H_{MF,kx}^2+H_{MF,ky}^2}\Big]\frac{\beta H_{MF,kx}}{\sqrt{H_{MF,kx}^2+H_{MF,ky}^2}}\times \\
&\qquad \exp\Big(-\beta H_{MF,kz}\cos\alpha_k\Big)\sin^2(\alpha_k)\,\mathrm{d}\alpha_k \\
\langle S_k\rangle_y &= \tfrac{2\pi T}{Z_k}\int_\alpha \; I_1\Big[-\beta\sin\alpha_k\sqrt{H_{MF,kx}^2+H_{MF,ky}^2}\Big]\frac{\beta H_{MF,ky}}{\sqrt{H_{MF,kx}^2+H_{MF,ky}^2}}\times \\
&\qquad \exp\Big(-\beta H_{MF,kz}\cos\alpha_k\Big)\sin^2(\alpha_k)\,\mathrm{d}\alpha_k \\
\langle S_k\rangle_z &= \tfrac{2\pi T}{Z_k}\int_\alpha \; I_0\Big[-\beta\sin\alpha_k\sqrt{H_{MF,kx}^2+H_{MF,ky}^2}\Big]\times \\
&\qquad \exp\Big(-\beta H_{MF,kz}\cos\alpha_k\Big)\beta H_{MF,kz}\cos\alpha_k\sin\alpha_k\,\mathrm{d}\alpha_k. \qquad (5.12)
\end{aligned}
$$

We have a total of 12 equations and 12 variables. While we are not able to solve this system analytically, a numerical solution has been obtained. To study the ZFC and FC temperature dependences of the moments, we use the Levenberg-Marquardt(LM) algorithm, [73] as described in section 5.1. We increment the temperature to T_i and start the algorithm using the solution of the previous T_{i-1} as a seed. In experiments, the FC and ZFC temperature scanning procedures were used. We will argue from the mean-field simulations that FC results in a metastable state, whereas ZFC creates a state closer to equilibrium.

The mean-field FC scans are started at high T and cooled in the field. In the second procedure, the simulation starts with the system in the equilibrium state at low T and is heated with H_z applied. This is similar to the experimental ZFC procedure in that the system starts from a state close to equilibrium. We will use the ZFC label for the mean-field procedure starting at low T in the equilibrium state.

For $J/(4j) = 2/3$, and $H_z/(4j) = 2.27\times10^{-4}$, we show typical results in Fig. 5.1 for average spin moments parallel (left) and perpendicular (right) to H_z vs T for $F/(4j) = -0.67$, 0 and 0.67 for both the FC and ZFC procedures. For this figure, and all the other figures in this section, the temperature scale T is normalized so that the FC transition for $J/(4j) = 2/3$ is at $T_C = 89.5$ K, the experimentally observed

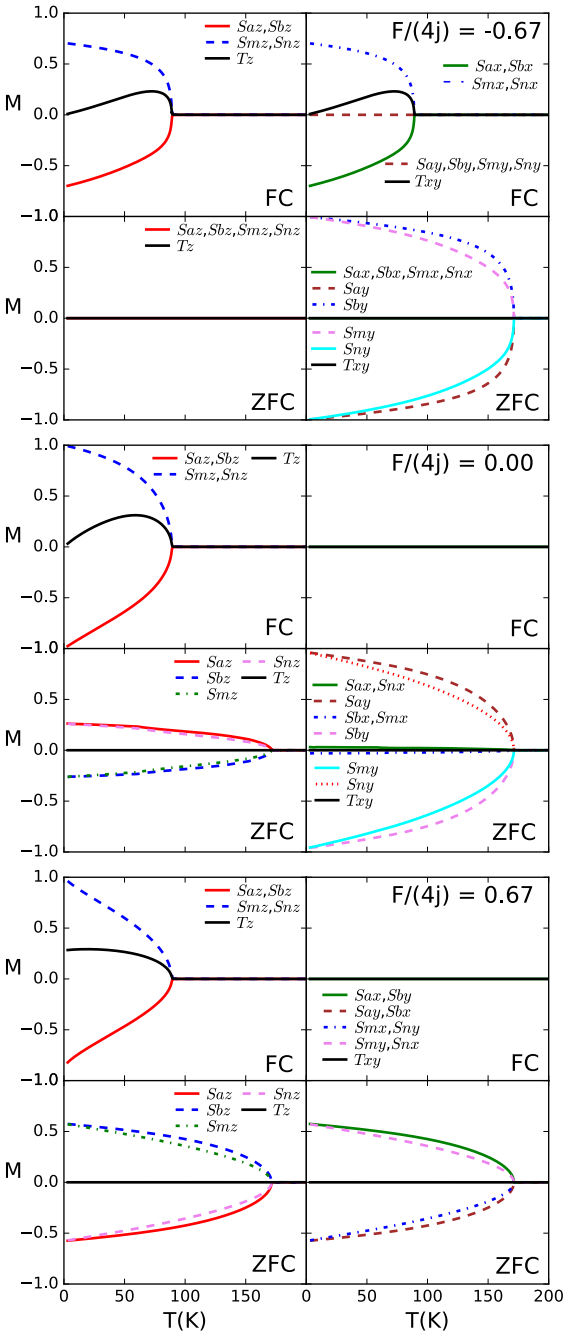

Figure 5.1: The average moments of each spin component as well as the net moment T_z along H and T_{xy} perpendicular to H, where H is an applied field equivalent to $H_z = 20$ Oe for FC and ZFC with $J/(4j) = 2/3$ and $F/(4j) = -0.67$, 0 and 0.67. In the ZFC procedure, the system is started in its ground state at low temperature. All interactions are antiferromagnetic.

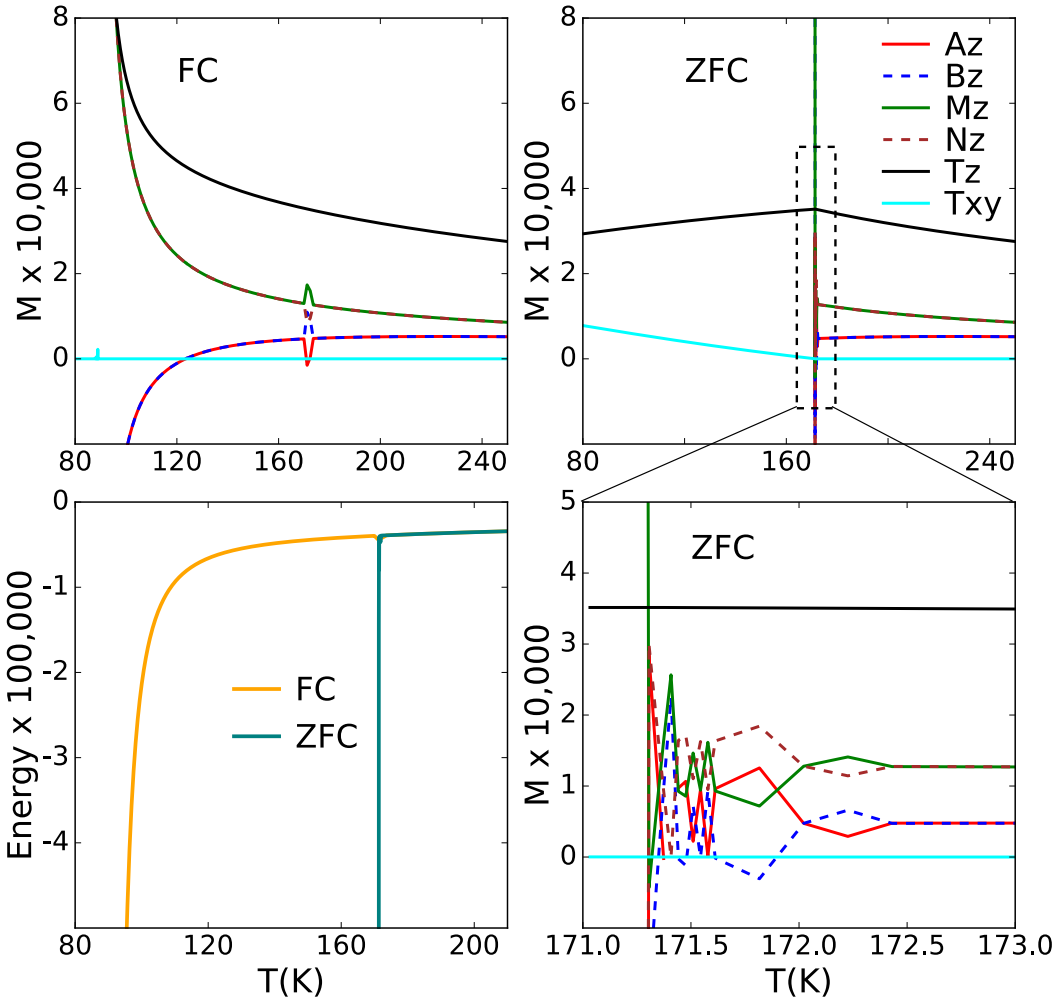

Figure 5.2: The behavior of the moments near T_{eq} for $J/(4j) = 2/3$, showing the polarization of the sublattices for FC and ZFC as well as the energy for FC and ZFC. The smooth growth of the FC ferrimagnetic moment contrasts to sharp SF transition observed in ZFC.

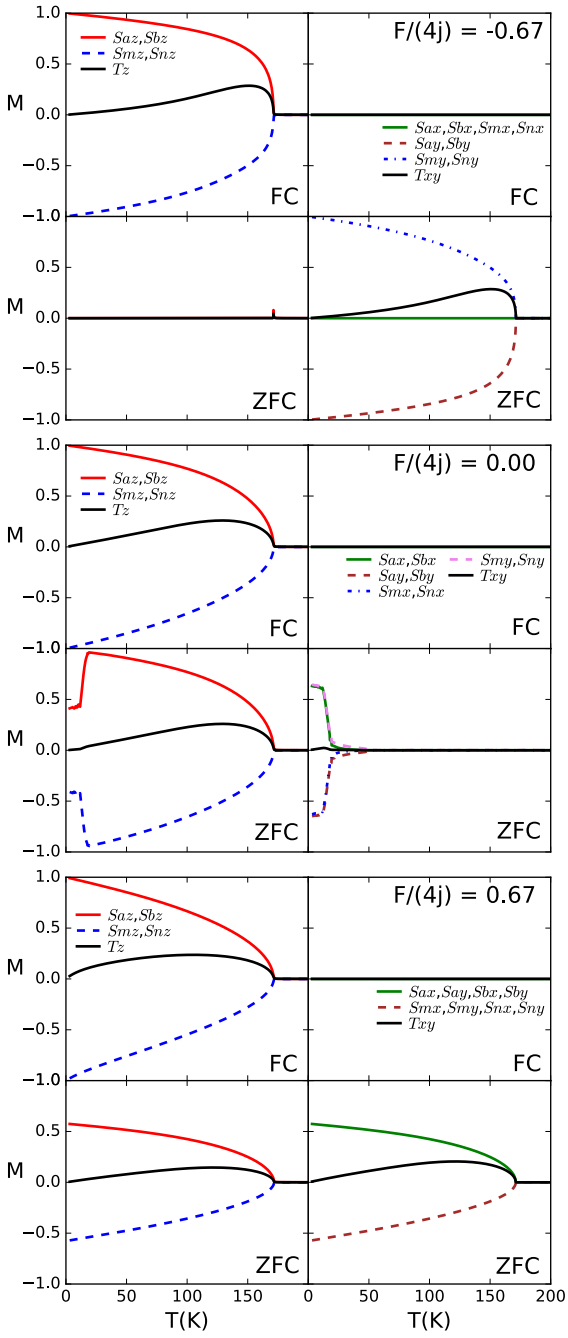

Figure 5.3: The average moments of each spin component as well as the net moment T_z along H and T_{xy} perpendicular to H, where H is an applied field equivalent to $H_z = 20$ Oe for FC and ZFC with $J/(4j) = -2/3$ and $F/(4j) = -0.67$, 0 and 0.67. The interactions are all antiferromagnetic except that between S_a and S_b which is ferromagnetic.

transition temperature for the net moment. The ZFC transitions occur at $T = T_{eq}$. The total moment along the magnetic field is $T_z = S_{az} + S_{bz} + S_{mz} + S_{nz}$ and total moment perpendicular to the field is $T_{xy} = \sqrt{\sum_{i \in x,y} \left(S_{ai} + S_{bi} + S_{mi} + S_{ni} \right)^2}$. For $F/(4j) = -0.67$, the equal moments on S_m and S_n are aligned with H_z and the equal moments on S_a and S_b are smaller and aligned opposite to H_z. This configuration yields a significant net moment along H_z for $T < T_C$. Above T_C, the very small moments induced by H_z on S_m and S_n are larger than those on S_a and S_b and this preference for the alignment of S_m and S_n gets locked in below T_C, despite the energy cost of having S_a and S_b aligned. This is clearly a metastable state. If the system starts from the ground state configuration, which is likely representing the ZFC state, S_a and S_b align in opposite directions, all spins align in an antiferromagnetic configuration, and no strong net moment develops.

For $F/(4j) = 0.67$, the FC behavior is similar for the net moment along H_z, but with a net moment growing more slowly below T_C and decreasing less at small T. The ZFC behavior, however, exhibits the BC2 state at low T, consistent with the ground state calculation. The BC2 state has its transition at a higher temperature, $T_{eq} \approx 170$ K. and it has no strong net moment parallel or perpendicular to H_z.

For $F = 0$, the FC behavior is intermediate between the $F/(4j) = -0.67$ and 0.67 cases, but the ZFC case shows a BC-type state with the higher transition temperature T_{eq}. Again, only FC shows a significant net moment along H_z. The metastable FC state is achieved when the LM algorithm settings suitably limit the explorable parameter space, as detailed in the appendix.

In the Fig 5.4 the effect of increased H_z field is visible. A typical rounding of the moment near T_C can be seen. This is the same behavior seen in experiment. The metastable state exists in higher fields as well.

The mean-field simulation cannot answer the question of whether the real system will achieve the equilibrium state upon FC or enter the metastable state. We can equilibrate the system in the simulation upon FC if we allow each iteration in temperature to sample a large enough region of parameter space. On the other hand, we know that the real LCO system shows strong hysteresis; FC results in a significant

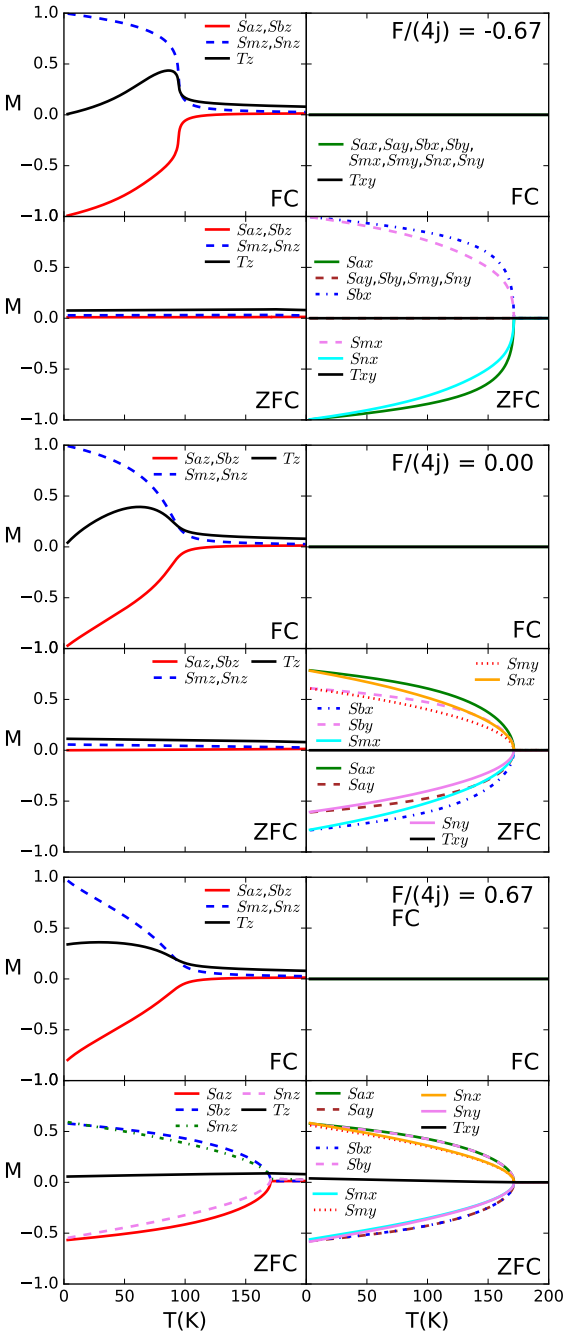

Figure 5.4: The average moments of each spin component as well as the net moment T_z along H and T_{xy} perpendicular to H, where H is an applied field equivalent to $H_z = 5$ kOe for FC and ZFC with $J/(4j) = 2/3$ and $F/(4j) = -0.67$, 0 and 0.67. In the ZFC procedure, the system is started in its ground state at low temperature. All interactions are antiferromagnetic.

net moment and ZFC produces a much reduced moment. This indicates that, for FC, the LCO system has a difficult time transforming from the state above T_{eq} to the equilibrium state is entered upon ZFC. The simulation results near T_{eq} indicate why this might be. Figure 5.2 shows the two configurations of spin moments obtained upon FC and ZFC for the case $F/(4j) = 0.67$. For ZFC, the system retains antiferromagnetic order for all $T \leq T_{eq}$, with S_b and S_m along H_z and S_a and S_n in the opposing direction. The four sublattice magnetizations nearly cancel for $T \leq T_{eq}$, as they also do for $T \geq T_{eq}$. Above T_{eq}, the small net magnetization decreases as T increases and the moments on S_m and S_n are significantly larger than those of S_a and S_b.

The FC situation for $T > T_{eq}$ is identical to the ZFC one. However, as T decreases below T_{eq}, the system cannot easily transition to the ZFC state. On both sides of the twin interface, the sublattices with S_m and S_n are more polarized along the field than the S_a and S_b sublattices. In order to reach the ZFC state, the entire sublattices on one side of the interface must reverse direction. The antiferromagnetic interactions between S_a and S_b can help facilitate the reversal, but it is not easy to achieve the reversal through short-range fluctuations in the same way that a uniform antiferromagnet would. In the latter case, independent regions of antiferromagnetically correlated regions fluctuate and grow in size near the transition temperature; the fluctuating regions do not have to compete against a field-induced bias favoring the alignment of one sublattice with the field over the other. In the interface case, the spins with the largest moments, S_m and S_n, do not interact directly and the bias created by the field throughout the lattices on each side of the interface opposes equilibration of the entire system. If the system does not equilibrate close to T_{eq}, it only becomes harder as T decreases because the field-induced bias of the sublattice moments increases. Although the field-induced bias at each site is small, the overall effect of the bias is strong because it permeates the entire system, effectively eliminating the ability of local fluctuations to reverse entire sublattices. Although S_a and S_b are not aligned, despite the antiferromagnetic interaction between them, the system orders at a temperature T_C, which is much lower than T_{eq}.

Although the mean-field simulation cannot equilibrate through thermal fluctu-

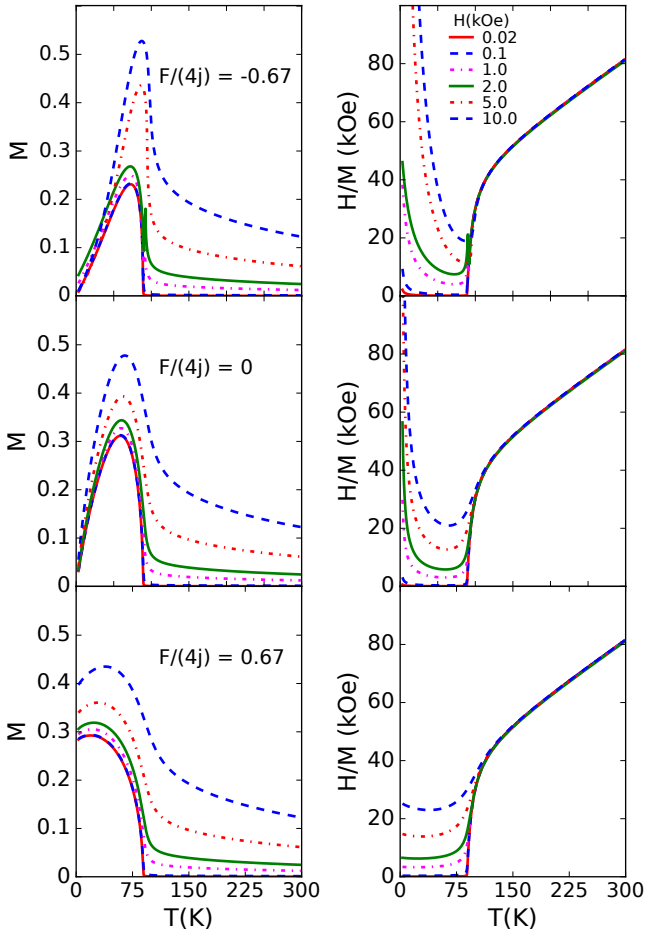

Figure 5.5: The net moment M and H/M vs T upon FC for several fields with $J/(4j) = 2/3$ and $F/(4j) = -0.67$, 0 and 0.67.

ations, upon each change in temperature we allow the system to vary the initial parameters within set limits. If these variations are allowed to be large enough, the the ZFC state, which is closer to equilibrium, can be achieved upon FC. The variation of one parameter affects an entire sublattice; that facilitates the reversal of that entire sublattice at once, eliminating the need for local fluctuations to grow against the field-induced bias for the S_m and S_n sublattices to align with the field.

For $T < T_{eq}$, the non-equilibrated FC system acts like a ferrimagnet with different moments on the two sublattices on either side of the interface. When T decreases to T_C, the system orders antiferromagnetically with the two unequal sublattice moments

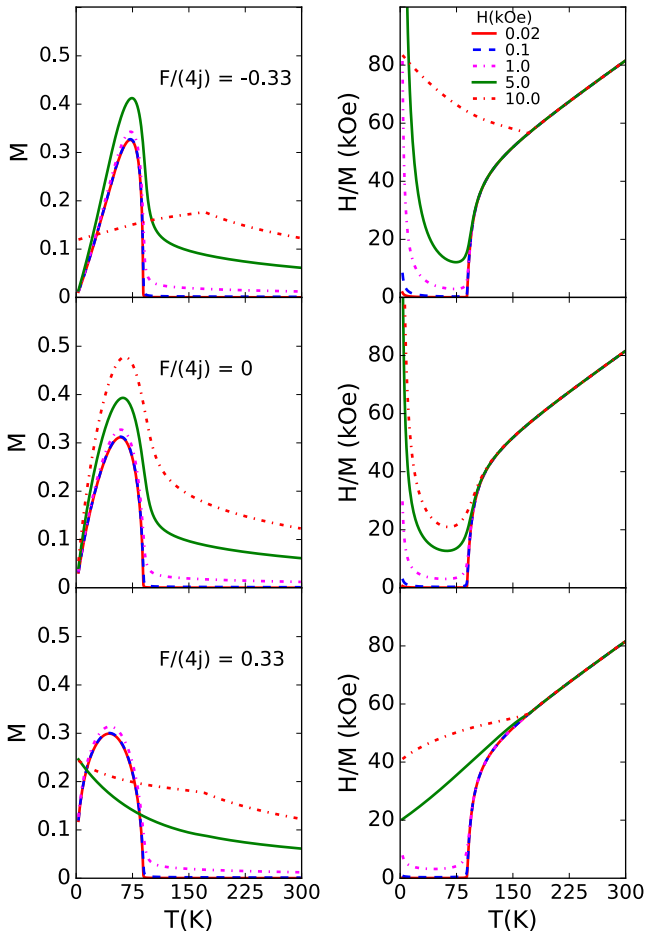

Figure 5.6: The net moment M and H/M vs T upon FC for several fields with $J/(4j) = 1/3$ and $F/(4j) = -0.33$, 0 and 0.33. The oxygen octahedra are now tilted with respect to the field. The tilt is 7.5°. For higher fields the metastable state is broken and spin-flop (SF) state appears.

creating a net moment. Unlike the ZFC antiferromagnetic transition that remains sharp at T_{eq} independent of the magnitude of H, the ferrimagnetic-like transition rounds with increasing H because the field directly couples to the order parameter as a result of the unequal sublattice moments. If the real LCO system does not, in fact, readily achieve equilibrium, one could expect FC behavior like that observed in this model.

We also examined the case where $J/(4j) = -2/3$, shown in Fig. 5.3, where the ferromagnetic interaction favors the alignment of S_a and S_b in the same direction for both the FC and ZFC procedures. In this case, because there is no conflict caused by the field-induced larger moments on sublattices S_m and S_n and the ferromagnetic J, the transition temperatures T_C and T_{eq}, for FC and ZFC, respectively, are nearly equal for all values of F. However, just as in the case for $J > 0$, H couples directly to the order parameter and the FC transition rounds rapidly as H increases. For ZFC, in contrast, the transition remains sharp as H increases. Unlike the $J > 0$ case, net moments occur for the ZFC case as well as for FC for $F \geq 0$ as a result of the unequal sublattice moments. Although the case $F < 0$ resembles the experiment, with a significant net moment only upon FC, the FC net moment decreases too rapidly with decreasing T to resemble the experiments. Because there is no reason to believe that the magnetic interaction is ferromagnetic for $\gamma = 165°$ in LCO, we only compare $J > 0$ to the experimental magnetization data in the remaining part of this section.

The FC behaviors produced in the mean-field calculations for $J/(4j) = 2/3$ and all F resemble the net moment observed in the FC for magnetization experiments that measure the net moment along the field. The suppression of the moment in the magnetization experiments [59] upon cooling in very small fields, $H \leq 3$ Oe, is also consistent with the ZFC calculations that show no significant net moment. For the polarized neutron scattering experiments, the fields at the sample were $H_z \geq 16$ Oe, so the sample was in the metastable state for all the measurements.

Figure 5.5 shows the net moment along H_z and H_z/M vs T for various fields upon cooling for $J/(4j) = 2/3$. The field is normalized using the Curie Law $M/H_z = C_m/T_m$ on an isolated spin with $g = 1$ and $S = 1$. The resulting conversion, $H_{kOe} = 1.47H_z$, ensures that the field strengths reasonably reflect those used in

the experiments. As H_z decreases, M vs T approaches an envelope below T_C that represents the spontaneous ordering. The transition is sharp near T_C for small H_z, but quickly rounds with increasing field. For H_z/M vs T, Curie-Weiss behavior is seen as a straight line above 150 K, and the net moment decreases H_z/M below T_C with rounding that increases rapidly for increasing H_z. This behavior mimics well that of the net moment observed in bulk LCO powders experiments, except that the experimental data include a large antiferromagnetic component from the bulk spins far from the interface that is not included in this model. Because the magnetization measurements [1, 53] do not indicate a large decrease in the net moment as T decreases towards zero, the behavior for $F > 0$ most resembles the experimental results, though it must be remembered that the mean-field approximation suppresses the thermal fluctuations that exist in the LCO system.

Simulations were also done for octahedra tilted with respect to the field (angle = 7.5° of tilt). Behavior seen is similar to the zero tilt simulations(see figure 5.6). For higher fields, the metastable state is broken in this simulation and the system jumps into ground state.

Results from the ground state $T = 0$ calculation using Eq. 5.4 are very close to those with finite T in Eq. 4.3, and the small T and H_z behavior from the mean-field calculation reflects the ground state results. These results indicate that the effective mean field represented by Eq. 5.4 is a good indicator of the behavior when cubic isotropy is broken by the tilted octahedral geometry though it does not precisely reflect a cubic anisotropy in the coordinates of the octahedra. The results were not significantly different from the case of untilted octahedra, so we conclude that the tilt is not a dominant factor in the behavior of LCO magnetic behavior.

Although we have presented most results for a specific value $J/(4j) = 2/3$ and some results with $J/(4j) = -2/3$, we found qualitatively similar for other values such as $J/(4j) = 4/3$ and $1/3$. The basic behavior does not seem sensitive to the magnitude of $J/(4j)$ chosen with $|J|$ comparable to, but larger than j.

5.1 Levenberg-Marquardt(LM) and limits

The Levenberg-Marquardt (LM) attempts to minimize

$$S(\mathbf{x}) = \sum_{i=1}^{12}(x_i - f_i(\mathbf{x}))^2 \tag{5.13}$$

for a given set of parameters. Equation 5.13 is minimized with $x_i = \langle S_k \rangle_j$ for $k \in a, b, m, n$ and $j \in x, y, z$, with $f_i = (T/Z_k)(\partial Z_k/\partial H_{MF,kj})$, representing a total of 12 equations and 12 variables. To first order,

$$S(\mathbf{x} + \boldsymbol{\sigma}) = \sum_{i=1}^{12}\Big(x_i - f_i(\mathbf{x}) - J_i\boldsymbol{\sigma}\Big)^2. \tag{5.14}$$

The Jacobian, $\mathbf{J}$, is calculated numerically. For this algorithm, two stopping criteria were set,

$$\frac{||\mathbf{D}(\mathbf{x}_k - \mathbf{x}_{k+1})||}{||\mathbf{D}(\mathbf{x}_{k+1})||} \leq XTOL, \tag{5.15}$$

where $\mathbf{D}$ is the diagonal matrix specifying the allowed scale of $\mathbf{x}$, and

$$\frac{||\mathbf{f}(\mathbf{x}_k)||}{||\mathbf{f}(\mathbf{x}_{k+1})||} \leq 1 + FTOL. \tag{5.16}$$

Here k indicates the step of the algorithm. We set XTOL = FTOL = 1.5×10^{-08}. Because LM finds only the local minimal, choosing the best initial $\mathbf{x}_0$ and $\mathbf{D}_0$ is paramount in determining whether the calculation finds the equilibrium or a metastable state. For ZFC, the SLSQP algorithm is used to find the global minimal state for $T = 0$. This state is then used as the initial $\mathbf{x}_0^0$ for the LM algorithm at finite T_0 for $T_0 > 0$. The scaling matrix is set to $\mathbf{D}_0^0 = |\mathbf{x}_0^0|$. The LM algorithm produces the value $\mathbf{x}_{final}^0$, which is the spin configuration at T_0 (the subscript $final$ indicates the final result of k iterations). For each T_{q+1} calculation, the previous result at T_q is used as the seed. For FC, we start at high T and decrease the temperature on each iteration, i.e $T_q < T_{q-1}$. For each T_q, the size of the initial step of LM algorithm is $\delta||\mathbf{D}_0^q\mathbf{x}_0^q||$ with $\delta = 1$ and $\mathbf{x}_0^q = \mathbf{x}_{final}^{q-1}$ is the spin configuration for previous T_{q-1}.

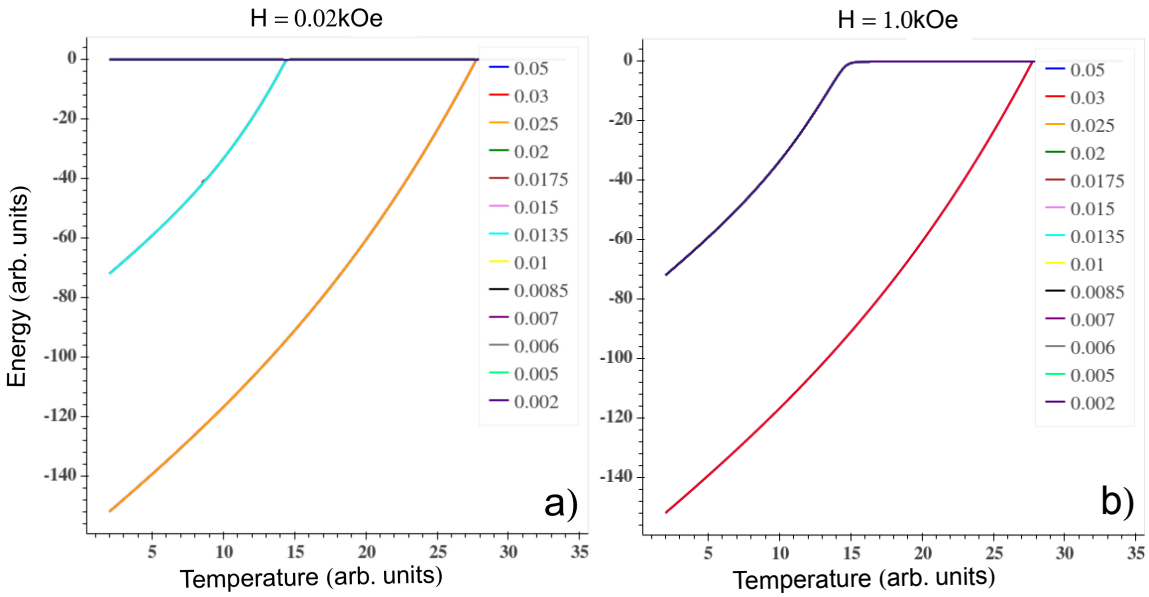

Figure 5.7: The energy of each spin configuration for each simulation graphed against temperature. Simulations for j = 15, J = 40, F = 0 are shown. For each simulation the number on the upper right panel is the floor (Ω) on the scaling matrix $\mathbf{D}_0$. This number Ω specifies the lowest possible scale on each spin value. If Ω is too low, for low field only the paramagnetic state is located. Specifying too high of a Ω allows the algorithm to find the true ground state. Only three lines are visible on graph a) and two lines are seen on graph b). That is because each line is graphed on top of the other. In graph a) the algorithm settles on a true ground state for $\Omega > 0.025$ or bigger. If $0.0135 < \Omega < 0.025$ the algorithm settles into a metastable state. For $\Omega < 0.0135$ the paramagnetic state is the final result. In graph b) for $\Omega > 0.03$ the metastable state is the final state.

The scaling matrix is $\mathbf{D}_0^q = |\mathbf{x}_0^q|$. Specifying $\mathbf{x}_0^q$ and $\mathbf{D}_0^q$ in this way constrains the parameter space so that the state is metastable, as observed in the LCO experiments. If the value of δ or minimal floor on $\mathbf{x}_0^q$ and $\mathbf{D}_0^q$ is increased, this results in a larger parameter space, corresponding to higher likelihood of finding the equilibrium state in FC. We experimented with different values for the floor on $\mathbf{x}_0^q$ and $\mathbf{D}_0^q$, to determine what parameters are necessary to achieve metastable state.

Looking at the equations 5.1 and 5.1, the full hamiltonian contains: quadratic terms $\overrightarrow{S_a} \cdot \overrightarrow{S_m}$, where spins couple with each other, linear terms, where spins couple with the field H_z and quartic terms, where coupling is with the anisotropy term F.

At high temperature the average value for each spin is low, quadratic and quartic terms disappear and linear term predominates. The magnetisation graph looks paramagnetic. So for high temperatures all the spins $\overrightarrow{S_a}$, $\overrightarrow{S_b}$ would be minimized to low values pointing in the same direction as the magnetic field. At each step the algorithm looks at the previous values of the spins and plugs them in as trial values for the next iteration. For the FC calculations the initial values of the spins is low and in the same direction as the field. At each iteration the algorithm described previously explores the phase space. If it is too constrained, the algorithm never leaves the paramagnetic state, the result can be seen in Fig. 5.7. Increasing the minimal floor (Ω) of the scaling matrix allows the algorithm to locate the metastable state or even jump into the true ground state. It is easier to go from paramagnetic state to a metastable state then to a ground state. For small fields and small average spins the coupling with 'J' and 'j' terms are suppressed and it is easier to establish a state with S_a and S_b oriented antiparallel to the field, coupling antiferromagnetically with S_m and S_n oriented parallel to the field. We believe this mimics the behavior of a true system, where thermal energy creates the same effect as the floor on the scaling matrix in the simulation. It is difficult for the system to jump from the metastable state to the ground state, because that requires the flipping of several spins at once. The twinning interfaces in the real system never exit the metastable state because to do so, the interacting spins on the entire lattice must flip all together.

5.1.1 Normalization

Converting temperature from our units to Kelvin, we used ferromagnetic signal that appears at 89.5 K [36]. Since we have the same signal in our simulations the conversion between our temperature T_m and kelvin T_K is $k_{trans} = T_m/T_K$. Converting Field values was move complicated. We created a simulation of independent spins interacting with the Field. Magnetization in such a system is given by

$$M_m = \frac{C_m}{T_m} B_m. \tag{5.17}$$

This is Curie's law and C is a Curie's constant. We got C = 0.3333 from the simulation. Maximum magnetization is $M_m = 1$, since there is only one interacting spin

with the field. For paramagnetic materials at low magnetic fields

$$C_A = \frac{\mu_B^2}{3k_B} N_A g^2 J(J+1)$$

where total angular momentum quantum number is assumed J = 1, g-factor g = 1 (assumption), k_B is the Boltzmann constant in SI units. Magnetization in relation to total electron spins is $M_A = N_A * \langle \mu \rangle$, where $\mu = gJ\mu_B$, and N_A is the Avogadro's number, μ_B is the Bohr magnetron. The Curie law in SI units

$$M_A = \frac{C_A}{T_A} B_A, \tag{5.18}$$

where T_A and B_A are in units of Tesla and Kelvin respectively. To get the ratio of B_A/B_m, we took the ratio of the two equations, $B_A/B_m = 0.147$ for J = 40. Division by a factor of 10 converts from Tesla to kOe.

Chapter 6

Conclusion

The mean-field calculation provides a plausible explanation for the observation of a significant net moment associated with critical-like behavior in LCO magnetization and neutron scattering experiments, its rapid rounding in relatively small fields, and the large difference in behavior for results obtained from the FC and ZFC procedures. The twin interface results in large interactions across the twin boundaries on half the sites with neighboring sites having no magnetic interaction. This asymmetry imposed on the sublattices enables a ferrimagnetic-like transition in the metastable state that rounds quickly with the field. One significant implication of the model is that LCO can exhibit a net moment in the absence of any ferromagnetic interaction between spins. Interactions described here would appear as short range ferromagnetic interactions as seen in neutron scattering measurements.[67]

Critical fluctuations are suppressed in mean-field models, and more sophisticated techniques might modify the physical picture derived in the present model. However, the apparent consistency between the mean-field model and the experimental observations, particularly the large differences between the behavior in FC and ZFC, suggest that the model captures much of the essence of the physics, which is that the asymmetric influence of the twin interface on the two antiferromagnetic sublattices results in a FC metastable state with a significant net moment.

LCO surfaces have a larger average value of γ than the interior. [29] The resulting strain is likely accommodated by twinning. Similarly, strain near impurity defects

can be released through high densities of twin interfaces. The large net moment observed LCO with large strain or defects is likely attributable to the induced twinning. Understanding the physical mechanism behind the appearance of a net moment in LCO is important in the design of thin-film devices using this material [**?** 62] and systems with similar properties.

The model presented here is for the net moment that forms near $T = 89$ K at twin interfaces in LCO. It does not address the behavior of the bulk moments in LCO. In particular, interesting behavior takes place as the temperature decreases to $T \approx 40$ K where the bulk magnetic moment decreases precipitously. [70, 53]. Modifications to this model can even explain surface and strain effects.

Chapter 7

Mirabo program

All of the images of the twinning interfaces were done on the program we designed that we call Mirabo (Images 3.1 3.2 3.3 3.4). It is a 3D visualization program to investigate the said interfaces. The program was originally written in C. The window and keyboard interface was accomplished through freeGLUT toolkit. It is a library of utilities for OpenGL programs that preform I/O with the operating system. Our original objective was to create the program that allows for the manipulation of the unit cell of a given compound.

We wanted to:

1. Rotate a unit cell
2. Create planes within the unit cell and orient such planes.
3. Erase specific atoms or groups of atoms
4. Clone a unit cell or clone individual atoms.
5. Measure the distances between individual atoms - to know the size of the bond.
6. Rotate/manipulate the cobalt octahedra within the unit cell - rotate it such that the orientation of the oxygen atoms with respect to cobalt and each other remains the same
7. Move the unit cell in xyz directions in small increments by using the keyboard.

8. Move the unit cell with respect to arbitrary coordinate system defined by the user - usually the coordinate system where a specified plane was defined by xy and z direction was perpendicular to this plane.
9. Manipulate multiple unit cells independent of each other.
10. Align two unit cells with respect to the atoms on the planes facing each other
11. Save the result for later work
12. Combine two results in two different files together
13. Save the image
14. Measure the Co-O-Co angle
15. Undo command
16. Change the color of specified atoms

There are other programs on the internet that can accomplish some of the items listed here: Mercury[74], Vesta[75], Jmol[76], VMD[77] and others. They all had certain deficiencies. Vesta and Mercury were not open source, so tweaking the program to my specifications was not possible. Mercury demanded registration and payment for many of its more advanced features. Jmol interface was clunky and did not allow me to specify planes. None would allow me to manipulate cobalt octahedra independent of the unit cell. Item 12 was not available in any program that we examined. None allowed me to manipulate the unit cell with respect to the specified plane (Vesta allowed it, but not using a keyboard interface - only through entering orientation and location numbers manually). Item 10 required access to the location of each atom and knowing how each location corresponds to the specified plane. The twinning interface required me to create the twins, combine them at the plane specified and then move each atom in to the optimal position so they overlay each other, while keeping their position with respect to their unit cell the same. To summarize, there

was no program on the internet that would allow us to accomplish all of this, so we wrote our own called Mirabo (working title).

The visualization style of Mirabo was based on Vesta, with a similar command structure. Color schemes for the atoms were borrowed from Jmol. Most of our work was done on the cif file from ICSD database diffraction data.[21] The openBabel program[78] was used to create a full unit cell and convert it to the *.xyz format.

One of the limitations of the FreeGlut toolkit is the inability to have a text output, a text input and an 3D crystal view for the structure on the same window. We had to utilize the terminal for input and output. This was inconvenient; it was difficult to see the unit cell when typing in commands. Seeing measurements of the bond angle and Co-O distance was also difficult; they only appeared in the terminal and not on the same window are the Unit cell image. The inconvenience of using the C language graphical user interface was also a problem. Eventually, we ported the program into Qt; it is a cross platform application framework, free and is designed for application software in C++. Instead of using structures in the C language, we now use objects from C++.

7.0.2 Organization

The organization of the program is based upon a collection of nested objects. Each unit cell is stored in an object called 'Unit Cell'. This object contains all the atoms in this unit cell as well as the basis vectors, planes within this unit cell, collection of methods to manipulate the unit cell.

Object 'Unit Cell' contains:

- vector array of 'Atom' objects
- vector array of 'Plane' objects
- Basis vectors for this unit cell
- Boolean parameters to enable:
  - display octahedra around the cobalt atoms with connected oxygen atoms

  - set this particular object to be active or not (that means when you are moving or manipulating it with mouse or a keyboard, other unit cells in the window remain stationary).
  - other internal parameters.

- Collection of methods to manipulate the given 'Unit Cell'
  - add_atom - add atom to the 'Unit Cell'
  - translate - translate the entire unit cell
  - rotate_all - rotate entire unit cell around a specified vector by a specified angle
  - setColor - set color for atoms of certain type (all 'La' atoms for example)
  - setRadii - set radii for atoms of certain type (all 'Co' atoms for example)
  - getPlane, setPlane - get or set a plane in this 'Unit Cell'.

Each atom is an object called 'Atom', with parameters:

- radius - double specifying radius of each atom
- color - a collection of three numbers referring to RBG color scheme
- type - string that refers to the type of an atom
- visible - boolean specifies whether the atom is visible or not.
- clicked - boolean specifies whether the atom has been clicked or not.

Each plane is an object called 'Plane', with parameters:

- Four vectors specifying four corners of the plane within the 'Unit Cell'
- RBG color of the plane
- active - boolean variable specifying whether the given plane is active (if a user is manipulating the unit cell with respect to a given plane, he/she has to see which plane it is.

7.0.3 Command input

The 3d image in the program window can be controlled by the mouse, keyboard, text input into a separate dialog box.

The mouse can be used to: rotate all the unit cells together around a specified plane (plane defined by the a,b basis vectors is the default), select a given atom - the position of this atom is then printed out the in the output text box. Clicking on several atoms in succession can be used to display distance between two atoms and angle between three atoms with respect to the middle atom. Selecting four atoms with a mouse and then clicking 'p' on the keyboard can be used to create a plane in the active unit cell.

The keyboard commands

- 'p' creates a plane
- 'd' deletes a plane
- 'q' moves all cells closer to screen
- 'w' moves all cells away from screen
- 'a' 'b' 'c' moves active cell in the direction of basis vectors
- 'A' 'B' 'C' same, but negative direction
- 'x' 'y' 'z' 'X' 'Y' 'Z' move active cell in the x,y,z direction
- 'j' 'k' 'l' ';' 'n' 'm' move active cell with respect to the specified plane. (n,m) moves it perpendicular to the specified plane
- '[' rotate unit cell such vector normal to the specified plane points in the y direction
- ']' normal vector points in the -y direction
- '-' bring two unit cells together on their planes.

- 'o' if two unit cells are touching on their specified planes, attempts to arrange the two cells, such that similar atoms are on arranged on top of each other - this command is used to optimize the interface between different unit cells for best fit.
- '(' delete all atoms above the specified plane in the specified unit cell
- ')' delete below
- 'U' un-delete atoms
- 'u' un-select atoms
- '\' undo
- arrow keys - rotate the unit cell with respect to specified plane (default is the plane specified by the basis vectors
- 'tab' toggle which unit cell is active at any one time
- 't' toggle which plane is active at any one time
- 'D' delete cell
- 'd' delete plane
- '=' show octahedra around the cobalt atom
- '_', '+' change the transparency of the octahedra
- 'e' 'r' 'g' 'h' ',' '.' moves individual selected atom within an active unit cell.
- 'del' deletes selected atom
- other internal commands

Text input box accepts text commands and can be used to enter bash shell on linux system if '!' is put before any text. Commands accepted so far:

- save - saves what is seen in a text file, as well as an image in a *.tga file
- load - loads a specified file
- import - if a file is already loaded, imports a new file into the same window.

Given more time, it is possible to greatly expand the Mirabo program. Those are some important methods that I thought is important to showcase in the code.

```
/*
        A point is rotated around an axis by an angle theta,
        This algorithm is used to rotate all atoms around a given axis.
        Each atom contains x,y,z coordinates
*/

Vec3d ArbitraryRotate(Vec3d point, double theta, Vec3d axis)
{
        Vec3d result;
        double p[3] = {point.x, point.y, point.z};
        double q[3];
        double r[3] = {axis.x, axis.y, axis.z};

        double costheta,sintheta;
        q[0] = 0;
        q[1] = 0;
        q[2] = 0;
   normalize(r);
   costheta = cos(theta*M_PI/180.0);
   sintheta = sin(theta*M_PI/180.0);

   q[0] += (costheta + (1 - costheta) * r[0] * r[0]) * p[0];
   q[0] += ((1 - costheta) * r[0] * r[1] - r[2] * sintheta) * p[1];
   q[0] += ((1 - costheta) * r[0] * r[2] + r[1] * sintheta) * p[2];

   q[1] += ((1 - costheta) * r[0] * r[1] + r[2] * sintheta) * p[0];
   q[1] += (costheta + (1 - costheta) * r[1] * r[1]) * p[1];
   q[1] += ((1 - costheta) * r[1] * r[2] - r[0] * sintheta) * p[2];
```

```
    q[2] += ((1 - costheta) * r[0] * r[2] - r[1] * sintheta) * p[0];
    q[2] += ((1 - costheta) * r[1] * r[2] + r[0] * sintheta) * p[1];
    q[2] += (costheta + (1 - costheta) * r[2] * r[2]) * p[2];



        result.x = q[0];
        result.y = q[1];
        result.z = q[2];
        return result;

}
```

One of the more complicated parts of the code was determining whether an atom has been clicked or not by the mouse.

```
/*
 * Point of closest approach is calculated
 * Vector is defined as A and B
 * Point is P
 * Q is the point on the AB vector, closest to P in euclidian space.
*/

Vec3d ClosestPoint(const Vec3d A, const Vec3d B, const Vec3d P)
{
    double t;
    Vec3d AB = B - A;
    double ab_square = AB * AB;
    Vec3d AP = P - A;
    double ap_dot_ab = AP * AB;
    // t is a projection param when we project vector AP onto AB
    t = ap_dot_ab / ab_square;
    // calculate the closest point
    Vec3d Q = A + AB * (t);
    return Q;
}



/*
```

```
 * Draws a vector starting from mouse x, y coordinates
 */
void windowToObjectf(int mouseX, int mouseY, Vec3d &begin, Vec3d &end)
{

    double modelViewMatrix[16], projectionMatrix[16];
    glGetDoublev( GL_MODELVIEW_MATRIX, modelViewMatrix );
    glGetDoublev( GL_PROJECTION_MATRIX, projectionMatrix);

    GLint viewport[4];
    glGetIntegerv( GL_VIEWPORT, viewport );


    double winX = (double)mouseX;

    double winY = viewport[3] - (double)mouseY;


    //xy screen coordinates are converted into xyz space coordinates.
    //0 indicates front of screen, 1 is the back of screen.
    gluUnProject(winX, winY, 0.0, modelViewMatrix,
                                  projectionMatrix, viewport,
                                  &begin.x, &begin.y, &begin.z);

    gluUnProject(winX, winY, 1.0, modelViewMatrix,
                                  projectionMatrix, viewport,
                                  &end.x, &end.y, &end.z);

}

int hitAtom(Unit_Cell &cell, int mouseX, int mouseY)
{
    Vec3d begin;
    Vec3d end;
    Vec3d Point;
    Vec3d Q;
```

```
    double norm;
    double max;
    int atom_hit = -1;  //return value if nothing is hit

//vector from front screen to back screen is calculated.
    windowToObjectf(mouseX, mouseY, begin, end);


    //loop rotates through all atoms.
    for(unsigned int i = 0; i < cell.backup.size(); i++)
    {


        Point = Vec3d(cell.backup[i].x, cell.backup[i].y,
                                                                cell

//closes approach to the center atom is calculated.
        Q = ClosestPoint(begin, end, Point);

//distance of closes approach.
     //if it is less then the radius of the atom, it is a hit.
        norm = (Point - Q).norm();


        if (norm < cell.backup[i].radius and
                  cell.backup[i].visible == true)
        {
            if(atom_hit < 0)
            {
                max = cell.backup[i].z;
                atom_hit = i;
            }
            else if(max < cell.backup[i].z)
            {
                max = cell.backup[i].z;
                atom_hit = i;
            }
```

```
        }
    }



    return atom_hit;  //atom number is returned.
}
```

Below are the structures for Atom and Plane; both are stored in the unit cell. There can be an arbitrary number of either.

```
 //xyz coordinates of the atom
struct Atom{double x; double y; double z;

    bool visible;      //is the atom visible
    bool clicked;     //has the atom been clicked

     //bonds linking this atom to others -
     //only relevant for the cobalt atom
    vector<int> bonds;

    //type of atom - Co, O, or La in my case,
    //generally specifies element type
    string type;

    //RGB color of the atom, each color 0-255 integer
    double paint[3];
    double radius;         //radius of the atom
};

struct Plane {

        /*
        * several points specifying the position of the plane,
        * the points are located on the edge of the unit cell,
        * given in xyz coordinates.
        */
```

```
    vector<Vec3d> edge;


        double paint[3];    //color of the plane is specified.
    bool selected;          //is the plane selected or not
};
```

This is the method that creates a plane. As you can see, it is only well defined if the lattice vectors exist. Once a plane exists, the given Unit cell can be rotated with respect to the plane, moved with respect to the plane or oriented with the normal vector to the plane pointing up (or down). These are useful operations if you want to superimpose two unit cells based on the individual planes. The edges are along the edges of the unit cell.

```
/*
 * Input is the unit cell,
 * an array answer which contain coordinates
 * of selected atoms to define a plane
 * output is a collection of Vec3d objects
 * to define the edges of the plane
*/
void makePlane(Unit_Cell &cell, int *answer, vector<Vec3d> &edge)
{
    //only three noncollinear atoms are necessary to define a plane
    Vec3d one;
    Vec3d two;  //second atom
    Vec3d position;  //third atom
    Vec3d cross;
    Vec3d zero = cell.getZero();
    Vec3d a = cell.getA();
    Vec3d b = cell.getB();
    Vec3d c = cell.getC();


    vector<Vec3d> initial;

    //two vectors that define the plane,
```

```
//answer[0] and answer[1], answer[2]
//contain the three atoms that define a plane
one = Vec3d(cell.backup[answer[0]].x - cell.backup[answer[1]].x,
            cell.backup[answer[0]].y - cell.backup[answer[1]].y,
            cell.backup[answer[0]].z - cell.backup[answer[1]].z);

two = Vec3d(cell.backup[answer[2]].x - cell.backup[answer[1]].x,
            cell.backup[answer[2]].y - cell.backup[answer[1]].y,
            cell.backup[answer[2]].z - cell.backup[answer[1]].z);

    //a point on the plane.
position = Vec3d(cell.backup[answer[1]].x,
                                        cell.backup[answer[1]].y,
                                        cell.backup[answer[1]].z);

    //vector normal to the plane
cross = crossProduct(one, two).normalized();


    //edge positions are calculated.
interPoint(zero, zero + a, position, cross, initial);
interPoint(zero, zero + b, position, cross, initial);
interPoint(zero + a, zero + b + a, position, cross, initial);
interPoint(zero + b, zero + a + b, position, cross, initial);

interPoint(zero, zero + c, position, cross, initial);
interPoint(zero + a, zero + a + c, position, cross, initial);
interPoint(zero + b, zero + b + c, position, cross, initial);
interPoint(zero + a + b, zero + a + b + c, position, cross, initial);

interPoint(zero + c, zero + a + c, position, cross, initial);
interPoint(zero + c, zero + c + b, position, cross, initial);
interPoint(zero + c + a, zero + b + a + c, position, cross, initial);
interPoint(zero + c + b, zero + a + b + c, position, cross, initial);

Vec3d store = Vec3d(0, 0, 0);
```

```
    for(unsigned int i = 0; i < initial.size(); i++)
    {
        store = store + initial[i];
    }
    store = store/initial.size();
    insertionSort(initial, store, cross);

    edge = initial;
}

/*
 * Method to calculate the edge positions of the plane
 * v1, v2 are input vectors define edges of the unit cell,
 *      cross is the normal vector to the plane
 *  initial stores the results.
*/
bool interPoint(Vec3d v1, Vec3d v2, Vec3d position,
                                Vec3d cross, vector<Vec3d> &initial)
{

        Vec3d ray = v2 - v1;
        if (fabs(ray*cross) == 0.0)
        {
            return false;
        }

        double t = -( cross*(v1 - position))/(cross*(ray));

        if(t >= -0.01 and t <= 1.01)
        {
            initial.push_back(v1 + t*(ray));
            return true;
        }

        return false;
}
```

```
/*
  * This class defines the object called Vec3d -
  *     which is just a 3 dimensional vector
  * with required operations
  * addition, subtraction, multiplication,
  * dot multiplication, division
  * and a cross product
*/

class Vec3d
{
    public:
        double x;
        double y;
        double z;

                //initialize a vector
        Vec3d (double ix, double iy, double iz)
                            { x = ix; y = iy; z = iz;}

        Vec3d (){x = 0; y = 0; z = 0;}
        Vec3d (const Vec3d &vec) {x = vec.x; y = vec.y; z = vec.z;}

                //add two vectors
        inline friend Vec3d operator+(const Vec3d &a, const Vec3d &b)
        {
            return Vec3d(a.x + b.x, a.y + b.y, a.z + b.z);
        }

                //subtract two vectors
        inline friend Vec3d operator-(const Vec3d &a, const Vec3d &b)
        {
            return Vec3d(a.x - b.x, a.y - b.y, a.z - b.z);
        }

                //multiply a vector by a number
        inline Vec3d operator*(double mult)
```

```
{
    return Vec3d(this->x * mult, this->y * mult, this->z * mult);
}

        //divide a vector by a number
inline Vec3d operator/(double div)
{
    return Vec3d(this->x / div, this->y / div, this->z / div);
}

        //dot multiply two vectors
inline friend double operator*(const Vec3d a, const Vec3d b)
{
    return a.x * b.x + a.y * b.y + a.z * b.z;
}

        //multiply a vector by a number
inline friend Vec3d operator*(double mul, const Vec3d b)
{
    return Vec3d(b.x*mul, b.y*mul, b.z*mul);
}


        //Cross product of two vectors
Vec3d cross(Vec3d input)
{
    Vec3d answer;
    answer.x = this->y*input.z - this->z*input.y;
    answer.y = -(this->x*input.z - this->z*input.x);
    answer.z = this->x*input.y - this->y*input.x;

    return answer;
}

        //establish equality
inline friend bool operator==(Vec3d one, Vec3d two)
{
```

```
            if(one.x != two.x) return false;
            if(one.y != two.y) return false;
            if(one.z != two.z) return false;

            return true;
        }

        //returns a euclidean norm of a vector.
        inline double norm() { return sqrt(x*x + y*y + z*z);}



                //returns a normalized vector
        inline void normalize()
        {
            x = x/norm();
            y = y/norm();
            z = z/norm();
        }

        inline Vec3d normalized()
        {
            return Vec3d (x/norm(), y/norm(), z/norm());
        }
                //prints the vector
        inline void show()
        { cout << "x: " << this->x <<
                        "y:" << this->y << "z:" << this->z << '\n';}
};
```

Code to save an image seen on the screen

```
/*
 * Saves a screenshot of the screen into a *.tga file
 * Most of this code was taken and modified
 * from an anonymous source on stack exchange.
*/

bool save_screenshot(string filename, unsigned int w, unsigned int h)
```

```
{
  //This prevents the images getting padded
 // when the width multiplied by 3 is not a multiple of 4
  glPixelStorei(GL_PACK_ALIGNMENT, 1);

  int nSize = w*h*3;
  // First let's create our buffer, 3 channels per Pixel
  char* dataBuffer = (char*)malloc(nSize*sizeof(char));

  if (!dataBuffer) return false;

   // Let's fetch them from the backbuffer
   // We request the pixels in GL_BGR format,
   glReadPixels((GLint)0, (GLint)0,
        (GLint)w, (GLint)h,
         GL_BGR, GL_UNSIGNED_BYTE, dataBuffer);

   //Now the file creation
   FILE *filePtr = fopen(filename.c_str(), "wb");
   if (!filePtr) return false;

   unsigned char rem_w = (unsigned char)(w%256);
   unsigned char rem_h = (unsigned char)(h%256);
   unsigned char div_w = (unsigned char)(w/256);
   unsigned char div_h = (unsigned char)(h/256);


   unsigned char TGAheader[12]={0,0,2,0,0,0,0,0,0,0,0,0};
   unsigned char header[6] = { rem_w, div_w,
                   rem_h, div_h,
                   24,0};
   // write the headers
   fwrite(TGAheader,     sizeof(unsigned char),  12,      filePtr);
   fwrite(header,        sizeof(unsigned char),  6,       filePtr);
   // finally our image data
   fwrite(dataBuffer,    sizeof(GLubyte),        nSize,   filePtr);
   fclose(filePtr);
```

```
  return true;
}
```

Chapter 8

Ground state minimizer

To find the ground state, we minimize Eq. 4.1, 4.2, and 4.3 with a local minimization algorithm SLSQP (Sequential Least SQuares Programming) from the SciPy package [73].

For a given $\mathcal{H}$, SLSQP constructs a Lagrangian

$$\mathcal{L}(\mathbf{x}, \sigma_1 ... \sigma_4) = \mathcal{H}(\mathbf{x}) - \sum_{i=1}^{4} \mu_i^T c_i(\mathbf{x}), \tag{8.1}$$

where the σ_i are Lagrange multipliers, [79] and equations of constraint are $c_i(\mathbf{x}) = 1 - \sqrt{S_{ix}^2 + S_{iy}^2 + S_{iz}^2}$. What happens afterwards is essentially a newton's method iteration, with the second derivative being set to zero each time. At each iterate $\mathbf{x}_{k+1} = \mathbf{x}_k + p$,

$$\begin{aligned} \min_{p} \quad & \nabla\mathcal{H}(\mathbf{x}_k)^T\mathbf{p} + \tfrac{1}{2}\mathbf{p}^T\nabla_{xx}^2\mathcal{L}(\mathbf{x}_k, \sigma)\mathbf{p} \\ \text{s.h.} \quad & c_i(\mathbf{x}_k) + \nabla c_i(\mathbf{x}_k)^T p = 0 \end{aligned} \tag{8.2}$$

This problem has a unique solution:

$$\nabla_{xx}^2\mathcal{L}(\mathbf{x}_k, \sigma)\mathbf{p} + \nabla\mathcal{H}(\mathbf{x}_k) - \sum_{i=0}^{4} \sigma_i \nabla c_i(\mathbf{x}_k) = 0$$

$$\nabla c_i(\mathbf{x}_k)\mathbf{p} + c_i = 0 \tag{8.3}$$

This is a condensed way to write 16 equations and unknowns. This system is solvable. At each iterate $\mathbf{x}_{k+1} = \mathbf{x}_k + \mathbf{p}$, $\mu_i = \sigma_i$. Stopping criteria is $|\mathcal{H}(\mathbf{x}_k) - \mathcal{H}(\mathbf{x}_{k+1})| < 10^{-8}$. To improve the speed and accuracy, $\nabla\mathcal{H}(\mathbf{x})$ and $\nabla c_i(\mathbf{x})$ were calculated analytically.

$$\begin{aligned}
\frac{\partial c_a(\mathbf{x})}{\partial S_{ax}} &= -\frac{2S_{ax}}{\sqrt{S_{ax}^2 + S_{ay}^2 + S_{az}^2}} \\
\frac{\partial c_a(\mathbf{x})}{\partial S_{ay}} &= -\frac{2S_{ay}}{\sqrt{S_{ax}^2 + S_{ay}^2 + S_{az}^2}} \\
\frac{\partial c_a(\mathbf{x})}{\partial S_{az}} &= -\frac{2S_{az}}{\sqrt{S_{ax}^2 + S_{ay}^2 + S_{az}^2}}
\end{aligned}$$

$$\begin{aligned}
\frac{\partial c_a(\mathbf{x})}{\partial S_{bx}}, \frac{\partial c_a(\mathbf{x})}{\partial S_{by}}, \frac{\partial c_a(\mathbf{x})}{\partial S_{bz}} &= 0 \\
\frac{\partial c_a(\mathbf{x})}{\partial S_{mx}}, \frac{\partial c_a(\mathbf{x})}{\partial S_{my}}, \frac{\partial c_a(\mathbf{x})}{\partial S_{mz}} &= 0 \\
\frac{\partial c_a(\mathbf{x})}{\partial S_{nx}}, \frac{\partial c_a(\mathbf{x})}{\partial S_{ny}}, \frac{\partial c_a(\mathbf{x})}{\partial S_{nz}} &= 0
\end{aligned} \tag{8.4}$$

Similar pattern follows to find ∇c_k for $k \in b, m, n$. To remind the reader how $\mathcal{H}$ and $\mathbf{M}$ look like:

$$\begin{aligned}
\mathcal{H} \;=\; & 4j\overrightarrow{S_a} \cdot \overrightarrow{S_m} + 4j\overrightarrow{S_b} \cdot \overrightarrow{S_n} + J\overrightarrow{S_a} \cdot \overrightarrow{S_b} \\
& -H_z\Big(S_{az} + S_{bz} + S_{mz} + S_{nz}\Big) \\
& +F \sum_{i\in x,y,z} \left(\sum_{k\in a,n} \left[\mathbf{M_1}\overrightarrow{S_k}\right]_i^4 \right) \\
& +F \sum_{i\in x,y,z} \left(\sum_{k\in b,m} \left[\mathbf{M_2}\overrightarrow{S_k}\right]_i^4 \right)
\end{aligned} \tag{8.5}$$

$$\mathbf{M}_1^{-1}(\alpha_0) = \begin{bmatrix} \cos\alpha_0 & \sin\alpha_0\cos\alpha_0 & \sin\alpha_0 \\ \sin\alpha_0 & \cos\alpha_0 & 0 \\ -\sin\alpha_0\cos\alpha_0 & \sin^2\alpha_0 & \cos\alpha_0 \end{bmatrix}$$

Taking the derivative with respect to S_{ax}

$$\begin{aligned}\frac{\partial \mathcal{H}}{\partial S_{ax}} &= 4jS_{ax}S_{mx} + JS_{ax}S_{bx} + \\ &\quad 4F\left(\left[\mathbf{M_1}\overrightarrow{S_a}\right]_x^3 \cos(\alpha_0)^2 - \left[\mathbf{M_1}\overrightarrow{S_a}\right]_y^3 \cos(\alpha_0)\sin(\alpha_0) + \left[\mathbf{M_1}\overrightarrow{S_a}\right]_z^3 \sin(\alpha_0)\right)\end{aligned} \quad (8.6)$$

The rest of 11 derivatives follow the same pattern. Analytic calculation of derivatives enables for faster and more accurate calculations of the minima.

Since SLSQP is a local minimizer, a combination of several initial seeds are used to find the global minimum and avoid the calculation from being trapped in local minima.

Chapter 9

Integrals

Integrals in Eq. 5.12 are solved numerically. Originally python 'quad' algorithm from scipy.optimize package [73] was used, but it was slow and could not deal with singular points properly. We ported the code into c language and used GNU scientific library. [80] for numerical calculations of integrals. Interface between c language and python was accomplished by wrapping c functions through ctypes foreign function library. Instead of 'quad' algorithm we now use a combination of QAG adaptive integration and QAGP adaptive integration with known singular points for difficult regions; the algorithms [81] are implemented in the GNU scientific library. [80].

Integrals in Eq. 5.12 contain and exponential and a Bessel function, large values in either can result in numerical overflow. The maximal value that a c double can store is approximately 1.8×10^{308}, this corresponds to ≈ 709 max value in the exponential. In our calculations such values are common. We experimented with cubic anisotropy values of F > 300, magnetic interactions J, $j > 200$ or more and $|H| > 400$. This can easily result in exponent > 700, while the ratio

$$\frac{1}{Z_k}\frac{\partial Z_k}{\partial H_{MF,ki}} < 1 \tag{9.1}$$

We dealt with the overflow problem by finding the largest possible value that the integrand in Eq. 5.12 can take and factoring it out. GNU scientific library [80] contains methods `sf_bessel_I0_scaled`, `sf_bessel_I1_scaled` to calculate exponentially scaled Bessel functions. Let I_{s0}, I_{s1} stand for scaled Bessel functions and I_0, I_1

for regular, then $I_{s0}(z) = I_0(z)e^{-z}$ is the conversion. Rewriting Eq. 5.12 as

$$\begin{aligned}
\langle S_k \rangle_x &= C_{kx} \frac{\int_\alpha I_{s1}\left[P_k \sin\alpha_k\right] e^{P_k \sin\alpha_k + Q_k \cos\alpha_k} \sin^2\alpha_k \, \mathrm{d}\alpha_k}{\int_\alpha I_{s1}\left[P_k \sin\alpha_k\right] e^{P_k \sin\alpha_k + Q_k \cos\alpha_k} \sin\alpha_k \, \mathrm{d}\alpha_k} \\
\langle S_k \rangle_y &= C_{ky} \frac{\int_\alpha I_{s1}\left[P_k \sin\alpha_k\right] e^{P_k \sin\alpha_k + Q_k \cos\alpha_k} \sin^2(\alpha_k) \, \mathrm{d}\alpha_k}{\int_\alpha I_{s1}\left[P_k \sin\alpha_k\right] e^{P_k \sin\alpha_k + Q_k \cos\alpha_k} \sin\alpha_k \, \mathrm{d}\alpha_k} \\
\langle S_k \rangle_z &= C_{kz} \frac{\int_\alpha I_{s1}\left[P_k \sin\alpha_k\right] e^{P_k \sin\alpha_k + Q_k \cos\alpha_k} \sin\alpha_k \cos\alpha_k \, \mathrm{d}\alpha_k}{\int_\alpha I_{s1}\left[P_k \sin\alpha_k\right] e^{P_k \sin\alpha_k + Q_k \cos\alpha_k} \sin\alpha_k \, \mathrm{d}\alpha_k}
\end{aligned} \tag{9.2}$$

with

$$\begin{aligned}
P_k &= \beta\sqrt{H_{MF,kx}^2 + H_{MF,ky}^2} \\
Q_k &= \beta H_{MF,kz}^2
\end{aligned} \tag{9.3}$$

and

$$\begin{aligned}
C_{kx} &= \frac{2\pi H_{MF,kx}}{P_k} \\
C_{ky} &= \frac{2\pi H_{MF,ky}}{P_k} \\
C_{kz} &= 2\pi Q_k
\end{aligned} \tag{9.4}$$

Rewriting the integrals

$$
\begin{aligned}
\langle S_k \rangle_x &= C_{kx} \frac{\int_{-1}^{1} I_{s1}\left[P_k\sqrt{1-x^2}\right] e^{P_k\sqrt{1-x^2}+Q_k x}\sqrt{1-x^2}\,\mathrm{d}x}{\int_{-1}^{1} I_{s0}\left[P_k\sqrt{1-x^2}\right] e^{P_k\sqrt{1-x^2}+Q_k x}\,\mathrm{d}x} \\
\langle S_k \rangle_x &= C_{ky} \frac{\int_{-1}^{1} I_{s1}\left[P_k\sqrt{1-x^2}\right] e^{P_k\sqrt{1-x^2}+Q_k x}\sqrt{1-x^2}\,\mathrm{d}x}{\int_{-1}^{1} I_{s0}\left[P_k\sqrt{1-x^2}\right] e^{P_k\sqrt{1-x^2}+Q_k x}\,\mathrm{d}x} \\
\langle S_k \rangle_x &= C_{kz} \frac{\int_{-1}^{1} I_{s0}\left[P_k\sqrt{1-x^2}\right] e^{P_k\sqrt{1-x^2}+Q_k x} x\,\mathrm{d}x}{\int_{-1}^{1} I_{s0}\left[P_k\sqrt{1-x^2}\right] e^{P_k\sqrt{1-x^2}+Q_k x}\,\mathrm{d}x}
\end{aligned}
\tag{9.5}
$$

For numerical overflow the problematic term is the exponent $P_k\sqrt{1-x^2}+Q_k x$. The biggest it can be is $\sqrt{P_k^2+Q_k^2}$ for $x = \frac{Q_k}{P_k^2+Q_k^2}$. The solution was simple: if $\sqrt{P_k^2+Q_k^2} > 700$ a correction term $D = \sqrt{P_k^2+Q_k^2}$ was subtracted from the exponent of all the integrands in Eq. 9.5. Furthermore the integrals were subdivided into smaller intervals around $x = \frac{Q_k}{P_k^2+Q_k^2}$ to ensure a more accurate integration close to the peak.

Looking at Eq. 9.5, for values $x = 0$ and $x = 1, -1$ the behaviour can become singular. We used QAGP adaptive integration [80] around those points. In all the integrals the denominator was better behaved then the numerator, for all reasonable values of P_k and Q_k the denominator doesn't have zeros at all nor sharp peaks greater then the numerator. In certain special cases (if numerator suddenly crashed to zero) we used CQUAD algorithm [82] to integrate Eq. 9.5.

Bibliography

[1] J.-Q. Yan, J.-S. Zhou, and J. B. Goodenough. Ferromagnetism in $LaCoO_3$. *Phys. Rev. B*, 70:014402, Jul 2004.

[2] Michael Grätzel. The light and shade of perovskite solar cells. *Nature materials*, 13(9):838–842, 2014.

[3] Haifeng Liu, Lei Shi, Shiming Zhou, Jiyin Zhao, Yuqiao Guo, Cailin Wang, and Laifa He. Simple polymer assisted deposition and strain-induced ferromagnetism of $LaCoO_3$ epitaxial thin films. *Surface and Coatings Technology*, 226:108 – 112, 2013.

[4] VV Lazenka, Gufei Zhang, Johan Vanacken, II Makoed, AF Ravinski, and VV Moshchalkov. Structural transformation and magnetoelectric behaviour in $Bi_{1-x}Gd_xFeO_3$ multiferroics. *Journal of Physics D: Applied Physics*, 45(12):125002, 2012.

[5] Per Erik Vullum, Hilde Lea Lein, M-A Einarsrud, Tor Grande, and Randi Holmestad. Tem observations of rhombohedral and monoclinic domains in $LaCoO_3$-based ceramics. *Philosophical Magazine*, 88(8):1187–1208, 2008.

[6] Rainer Schmidt, J. Wu, C. Leighton, and I. Terry. Dielectric response to the low-temperature magnetic defect structure and spin state transition in polycrystalline $LaCoO_3$. *Phys. Rev. B*, 79:125105, Mar 2009.

[7] M. W. Haverkort, Z. Hu, J. C. Cezar, T. Burnus, H. Hartmann, M. Reuther, C. Zobel, T. Lorenz, A. Tanaka, N. B. Brookes, H. H. Hsieh, H.-J. Lin, C. T.

Chen, and L. H. Tjeng. Spin state transition in $lacoo_3$ studied using soft x-ray absorption spectroscopy and magnetic circular dichroism. *Phys. Rev. Lett.*, 97:176405, Oct 2006.

[8] O Toulemonde, N N'Guyen, F Studer, and A Traverse. Spin state transition in $LaCoO_3$ with temperature or strontium doping as seen by XAS. *Journal of Solid State Chemistry*, 158(2):208–217, 2001.

[9] Wikimedia Commons. Superexchange mechanism, 2007.

[10] Alberta Bonanni and Tomasz Dietl. A story of high-temperature ferromagnetism in semiconductors. *Chemical Society Reviews*, 39(2):528–539, 2010.

[11] Wikimedia Commons. Double exchange mechanism, 2006.

[12] E Pavarini, E Koch, F Anders, and M Jarrell. Correlated electrons: from models to materials. *Reihe Modeling and Simulation*, 2, 2012.

[13] Natal'ya Borisovna Ivanova, Sergei Gennad'evich Ovchinnikov, Maksim Mikhailovich Korshunov, Ilya Mikhailovich Eremin, and Natal'ya Valer'evna Kazak. Specific features of spin, charge, and orbital ordering in cobaltites. *Physics-Uspekhi*, 52(8):789–810, 2009.

[14] Y Lee and BN Harmon. Rhombohedral distortion effects on electronic structure of $LaCoO_3$. *Journal of Applied Physics*, 113(17):17E145, 2013.

[15] Shiming Zhou, Laifa He, Shuangyi Zhao, Yuqiao Guo, Jiyin Zhao, and Lei Shi. Size-dependent structural and magnetic properties of $lacoo_3$ nanoparticles. *The Journal of Physical Chemistry C*, 113(31):13522–13526, 2009.

[16] S Park, P Ryan, E Karapetrova, JW Kim, JX Ma, J Shi, JW Freeland, and Weida Wu. Microscopic evidence of a strain-enhanced ferromagnetic state in $lacoo_3$ thin films. *Applied Physics Letters*, 95(7):072508, 2009.

[17] Oak Ridge National Laboratory. Polarized triple-axis spectrometer, 1999.

[18] Ross Stewart. Polarized neutrons. University Lecture, 2011.

[19] G. Bannasch and W. Selke. Heisenberg antiferromagnets with uniaxial exchange and cubic anisotropies in a field. *The European Physical Journal B*, 69(3):439–444, 2009.

[20] T-C Dinh and R Folk. Ground states of anisotropic antiferromagnets with single ion and cubic anisotropy. *arXiv preprint arXiv:0907.1480*, 2009.

[21] G Thornton, BC Tofield, and AW Hewat. A neutron diffraction study of $LaCoO_3$ in the temperature range $4.2 < T < 1248$ k. *Journal of Solid State Chemistry*, 61(3):301–307, 1986.

[22] W.C. Koehler and E.O. Wollan. Neutron-diffraction study of the magnetic properties of perovskite-like compounds $LaBO_3$. *Journal of Physics and Chemistry of Solids*, 2(2):100 – 106, 1957.

[23] N Menyuk, K Dwight, and PM Raccah. Low temperature crystallographic and magnetic study of $LaCoO_3$. *Journal of Physics and Chemistry of Solids*, 28(4):549–556, 1967.

[24] A Podlesnyak, Margarita Russina, Albert Furrer, Aleksei Alfonsov, Eugenia Vavilova, Vladislav Kataev, Bernd Büchner, Th Strässle, Ekaterina Pomjakushina, Kazimierz Conder, et al. Spin-state polarons in lightly-hole-doped $LaCoO_3$. *Physical review letters*, 101(24):247603, 2008.

[25] S Yamaguchi, Y Okimoto, H Taniguchi, and Y Tokura. Spin-state transition and high-spin polarons in $LaCoO_3$. *Physical Review B*, 53(6):R2926, 1996.

[26] C. Pinta, D. Fuchs, M. Merz, M. Wissinger, E. Arac, H. v. Löhneysen, A. Samartsev, P. Nagel, and S. Schuppler. Suppression of spin-state transition in epitaxially strained $LaCoO_3$. *Phys. Rev. B*, 78:174402, Nov 2008.

[27] Han Hsu, Peter Blaha, and Renata M. Wentzcovitch. Ferromagnetic insulating state in tensile-strained $lacoo_3$ thin films from lda + u calculations. *Phys. Rev. B*, 85:140404, Apr 2012.

[28] D Fuchs, E Arac, C Pinta, S Schuppler, R Schneider, and H v Löhneysen. Tuning the magnetic properties of la co o 3 thin films by epitaxial strain. *Physical Review B*, 77(1):014434, 2008.

[29] A M Durand, D P Belanger, T J Hamil, F Ye, S Chi, J A Fernandez-Baca, C H Booth, Y Abdollahian, and M Bhat. The unusual magnetism of nanoparticle lacoo$_3$. *Journal of Physics: Condensed Matter*, 27(17):176003, 2015.

[30] I. Fita, V. Markovich, D. Mogilyansky, R. Puzniak, A. Wisniewski, L. Titelman, L. Vradman, M. Herskowitz, V. N. Varyukhin, and G. Gorodetsky. Size- and pressure-controlled ferromagnetism in lacoo$_3$ nanoparticles. *Phys. Rev. B*, 77:224421, Jun 2008.

[31] K. Berggold, M. Kriener, P. Becker, M. Benomar, M. Reuther, C. Zobel, and T. Lorenz. Anomalous expansion and phonon damping due to the co spin-state transition in $r$coo$_3$ (r = La, pr, nd, and eu). *Phys. Rev. B*, 78:134402, Oct 2008.

[32] EL Nagaev and AI Podel'shchikov. Phase separation and resistivity jumps in co compounds and other materials with low-spin-high-spin transitions. *Journal of Physics: Condensed Matter*, 8(30):5611, 1996.

[33] Y Tokura, Y Okimoto, S Yamaguchi, H Taniguchi, T Kimura, and H Takagi. Thermally induced insulator-metal transition in lacoo 3: A view based on the mott transition. *Physical Review B*, 58(4):R1699, 1998.

[34] P.E. Vullum, R. Holmestad, H.L. Lein, J. Mastin, M.-A. Einarsrud, and T. Grande. Monoclinic ferroelastic domains in $LaCoO_3$-based perovskites. *Advanced Materials*, 19(24):4399–4403, 2007.

[35] D. Fuchs, L. Dieterle, E. Arac, R. Eder, P. Adelmann, V. Eyert, T. Kopp, R. Schneider, D. Gerthsen, and H. v. Löhneysen. Suppression of the ferromagnetic state in $LaCoO_3$ films by rhombohedral distortion. *Phys. Rev. B*, 79:024424, Jan 2009.

[36] Alice Durand. *The effects of synthesis, Sr-doping, and Co_3 O_4 on the perovskite $LaCoO_3$*. University of California, Santa Cruz, 2014.

[37] J Baier, S Jodlauk, M Kriener, A Reichl, C Zobel, H Kierspel, A Freimuth, and T Lorenz. Spin-state transition and metal-insulator transition in $La_{1-x}Eu_xCoO_3$. *Physical Review B*, 71(1):014443, 2005.

[38] V V Sikolenko, I O Troyanchuk, V V Efimov, E A Efimova, S I Tiutiunnikov, D V Karpinsky, S Pascarelli, O Zaharko, A Ignatov, D Aquilanti, A G Selutin, A N Shmakov, and D Prabhakaran. Exafs and x-ray diffraction study of $LaCoO_3$ across the spin-state transition. *Journal of Physics: Conference Series*, 712(1):012118, 2016.

[39] Y Jiang, F Bridges, N Sundaram, DP Belanger, IE Anderson, JF Mitchell, and H Zheng. Study of the local distortions of the perovskite system $La_{1-x}Sr_xCoO_3$ $(0x0.35)$ using the extended x-ray absorption fine structure technique. *Physical Review B*, 80(14):144423, 2009.

[40] R. Caciuffo, D. Rinaldi, G. Barucca, J. Mira, J. Rivas, M. A. Señarís Rodríguez, P. G. Radaelli, D. Fiorani, and J. B. Goodenough. Structural details and magnetic order of $la_{1-x}sr_xcoo_3$ ($x\<$ 0.3). *Phys. Rev. B*, 59:1068–1078, Jan 1999.

[41] CH Kim, JW Jang, SY Cho, IT Kim, and KS Hong. Ferroelastic twins in $LaAlO_3$ polycrystals. *Physica B: Condensed Matter*, 262(3):438–443, 1999.

[42] John B Goodenough. An interpretation of the magnetic properties of the perovskite-type mixed crystals $La_{1-x}Sr_xCoO_3$- λ. *Journal of Physics and Chemistry of Solids*, 6(2-3):287–297, 1958.

[43] M Abbate, JC Fuggle, A Fujimori, LH Tjeng, CT Chen, R Potze, GA Sawatzky, H Eisaki, and S Uchida. Electronic structure and spin-state transition of $LaCoO_3$. *Physical Review B*, 47(24):16124, 1993.

[44] MA Korotin, S Yu Ezhov, IV Solovyev, VI Anisimov, DI Khomskii, and

GA Sawatzky. Intermediate-spin state and properties of lacoo 3. *Physical Review B*, 54(8):5309, 1996.

[45] N Sundaram, Y Jiang, IE Anderson, DP Belanger, CH Booth, F Bridges, JF Mitchell, Th Proffen, and H Zheng. Local structure of la 1- x sr x coo 3 determined from exafs and neutron pair distribution function studies. *Physical review letters*, 102(2):026401, 2009.

[46] G Maris, Y Ren, V Volotchaev, C Zobel, T Lorenz, and TTM Palstra. Evidence for orbital ordering in lacoo 3. *Physical Review B*, 67(22):224423, 2003.

[47] Masayuki Itoh, Masaru Sugahara, Ikuomi Natori, and Kiyoichiro Motoya. Spin state and hyperfine interaction in $LaCoO_3$: Nmr and magnetic susceptibility studies. *Journal of the Physical Society of Japan*, 64(10):3967–3977, 1995.

[48] S. Noguchi, S. Kawamata, K. Okuda, H. Nojiri, and M. Motokawa. Evidence for the excited triplet of co^{3+} in $lacoo_3$. *Phys. Rev. B*, 66:094404, Sep 2002.

[49] Z. Ropka and R. J. Radwanski. ^5D term origin of the excited triplet in $LaCoO_3$. *Phys. Rev. B*, 67:172401, May 2003.

[50] Min Zhuang, Weiyi Zhang, and Naiben Ming. Competition of various spin states of lacoo 3. *Physical Review B*, 57(17):10705, 1998.

[51] M. Medarde, C. Dallera, M. Grioni, J. Voigt, A. Podlesnyak, E. Pomjakushina, K. Conder, Th. Neisius, O. Tjernberg, and S. N. Barilo. Low-temperature spin-state transition in $LaCoO_3$ investigated using resonant x-ray absorption at the co k edge. *Phys. Rev. B*, 73:054424, Feb 2006.

[52] Scott Medling, Yuen Lee, H Zheng, JF Mitchell, JW Freeland, Bruce N Harmon, and F Bridges. Evolution of magnetic oxygen states in sr-doped $LaCoO_3$. *Physical review letters*, 109(15):157204, 2012.

[53] A M Durand, D P Belanger, C H Booth, F Ye, S Chi, J A Fernandez-Baca, and M Bhat. Magnetism and phase transitions in $lacoo_3$. *Journal of Physics: Condensed Matter*, 25(38):382203, 2013.

[54] György Vankó, Frank MF de Groot, Simo Huotari, RJ Cava, Thomas Lorenz, and M Reuther. Intersite 4p-3d hybridization in cobalt oxides: a resonant x-ray emission spectroscopy study. *arXiv preprint arXiv:0802.2744*, 2008.

[55] G. E. Sterbinsky, P. J. Ryan, J.-W. Kim, E. Karapetrova, J. X. Ma, J. Shi, and J. C. Woicik. Local atomic and electronic structures of epitaxial strained $LaCoO_3$ thin films. *Phys. Rev. B*, 85:020403, Jan 2012.

[56] D. Fuchs, C. Pinta, T. Schwarz, P. Schweiss, P. Nagel, S. Schuppler, R. Schneider, M. Merz, G. Roth, and H. v. Löhneysen. Ferromagnetic order in epitaxially strained $LaCoo_3$ thin films. *Phys. Rev. B*, 75:144402, Apr 2007.

[57] I. Fita, D. Mogilyansky, V. Markovich, R. Puzniak, A. Wisniewski, L. Titelman, L. Vradman, M. Herskowitz, V.N. Varyukhin, and G. Gorodetsky. Pressure-induced suppression of ferromagnetic phase in lacoo3 nanoparticles. *Journal of Non-Crystalline Solids*, 354(4751):5204 – 5206, 2008. Non-Crystalline Solids 9Proceedings of the 9th International Workshop on Non-Crystalline Solids9th International Workshop on Non-Crystalline Solids.

[58] A Harada, T Taniyama, Y Takeuchi, T Sato, T Kyomen, and M Itoh. Ferromagnetism at the surface of a $LaCoO_3$ single crystal observed using scanning squid microscopy. *Physical Review B*, 75(18):184426, 2007.

[59] A M Durand, T J Hamil, D P Belanger, S Chi, F Ye, J A Fernandez-Baca, Y Abdollahian, and C H Booth. The effects of co_3O_4 on the structure and unusual magnetism of $lacoo_3$. *Journal of Physics: Condensed Matter*, 27(12):126001, 2015.

[60] Yang Wang and Hong Jin Fan. Orbital ordering-driven ferromagnetism in $LaCoO_3$ nanowires. *Journal of Applied Physics*, 108(5):053917, 2010.

[61] J. W. Freeland, J. X. Ma, and J. Shi. Ferromagnetic spin-correlations in strained $LaCoO_3$ thin films. *Applied Physics Letters*, 93(21):212501, 2008.

[62] Chengqing Hu, Keun Woo Park, Agham Posadas, Jean L Jordan-Sweet, Alexander A Demkov, and Edward T Yu. Voltage-controlled ferromagnetism and magnetoresistance in lacoo3/srtio3 heterostructures. *Journal of Applied Physics*, 114(18):183909, 2013.

[63] Jiansheg Wu and C Leighton. Glassy ferromagnetism and magnetic phase separation in la 1- x sr x coo 3. *Physical Review B*, 67(17):174408, 2003.

[64] C Zobel, M Kriener, D Bruns, J Baier, M Grüninger, T Lorenz, P Reutler, and A Revcolevschi. Evidence for a low-spin to intermediate-spin state transition in lacoo 3. *Physical Review B*, 66(2):020402, 2002.

[65] A. Podlesnyak, S. Streule, J. Mesot, M. Medarde, E. Pomjakushina, K. Conder, A. Tanaka, M. W. Haverkort, and D. I. Khomskii. Spin-state transition in $lacoo_3$: Direct neutron spectroscopic evidence of excited magnetic states. *Phys. Rev. Lett.*, 97:247208, Dec 2006.

[66] Svein Stølen, Fredrik Grønvold, Hendrik Brinks, Tooru Atake, and Hideki Mori. Energetics of the spin transition in lacoo 3. *Physical Review B*, 55(21):14103, 1997.

[67] Kichizo Asai, Osamu Yokokura, Nobuhiko Nishimori, Henry Chou, J. M. Tranquada, G. Shirane, Sadao Higuchi, Yuichiro Okajima, and Kay Kohn. Neutron-scattering study of the spin-state transition and magnetic correlations in $la_{1-x}sr_xcoo_3$ (x=0 and 0.08). *Phys. Rev. B*, 50:3025–3032, Aug 1994.

[68] M. Merz, P. Nagel, C. Pinta, A. Samartsev, H. v. Löhneysen, M. Wissinger, S. Uebe, A. Assmann, D. Fuchs, and S. Schuppler. X-ray absorption and magnetic circular dichroism of $lacoo_3$, $la_{0.7}ce_{0.3}coo_3$, and $la_{0.7}sr_{0.3}coo_3$ films: Evidence for cobalt-valence-dependent magnetism. *Phys. Rev. B*, 82:174416, Nov 2010.

[69] K Binder and PC Hohenberg. Surface effects on magnetic phase transitions. *Physical Review B*, 9(5):2194, 1974.

[70] D P Belanger, T Keiber, F Bridges, A M Durand, A Mehta, H Zheng, J F Mitchell, and V Borzenets. Structure and magnetism in $LaCoO_3$. *Journal of Physics: Condensed Matter*, 28(2):025602, 2016.

[71] A. Herklotz, A. D. Rata, L. Schultz, and K. Dörr. Reversible strain effect on the magnetization of $lacoo_3$ films. *Phys. Rev. B*, 79:092409, Mar 2009.

[72] M. Dudzinski, J. Sznajd, and J. Zittartz. Quantum spin model of a cubic ferromagnet in a magnetic field. *The European Physical Journal B - Condensed Matter and Complex Systems*, 17(4):575–579, 2000.

[73] Mark Galassi, Jim Davies, James Theiler, Brian Gough, Gerard Jungman, Michael Booth, and Fabrice Rossi. *Gnu Scientific Library: Reference Manual*. Lightning Source Inc, 2003.

[74] Clare F. Macrae, Ian J. Bruno, James A. Chisholm, Paul R. Edgington, Patrick McCabe, Elna Pidcock, Lucia Rodriguez-Monge, Robin Taylor, Jacco van de Streek, and Peter A. Wood. *Mercury CSD 2.0* – new features for the visualization and investigation of crystal structures. *Journal of Applied Crystallography*, 41(2):466–470, Apr 2008.

[75] Koichi Momma and Fujio Izumi. *VESTA3* for three-dimensional visualization of crystal, volumetric and morphology data. *Journal of Applied Crystallography*, 44(6):1272–1276, Dec 2011.

[76] Angel Herráez. *How to use Jmol to study and present molecular structures*, volume 1. Lulu. com, 2008.

[77] William Humphrey, Andrew Dalke, and Klaus Schulten. VMD – Visual Molecular Dynamics. *Journal of Molecular Graphics*, 14:33–38, 1996.

[78] Noel M O'Boyle, Michael Banck, Craig A James, Chris Morley, Tim Vandermeersch, and Geoffrey R Hutchison. Open babel: An open chemical toolbox. *Journal of cheminformatics*, 3(1):33, 2011.

[79] Jorge Nocedal and Stephen Wright. *Numerical optimization*. Springer Science & Business Media, 2006.

[80] Mark Galassi, Jim Davies, James Theiler, Brian Gough, Gerard Jungman, Michael Booth, and Fabrice Rossi. Gnu scientific library.

[81] Robert Piessens, Elise de Doncker-Kapenga, Christoph W Überhuber, and David K Kahaner. *QUADPACK: A subroutine package for automatic integration*, volume 1. Springer Science & Business Media, 2012.

[82] Pedro Gonnet. Increasing the reliability of adaptive quadrature using explicit interpolants. *ACM Transactions on Mathematical Software (TOMS)*, 37(3):26, 2010.